The surface energy balance in a cold-arid permafrost environment, Ladakh Himalaya, India

John Mohd Wani[1], Renoj J. Thayyen[2*], Chandra Shekhar Prasad Ojha[1], and Stephan Gruber[3]

[1]Department of Civil Engineering, Indian Institute of Technology (IIT) Roorkee, India, [2]Water Resources System Division, National Institute of Hydrology, Roorkee, India (renoj.nihr@gov.in; renojthayyen@gmail.com), [3]Department of Geography & Environmental Studies, Carleton University, Ottawa, Canada

Abstract

The cold-arid trans-Himalayan region comprises significant areas underlain by permafrost. While the information on the permafrost characteristics and extent started emerging, the governing energy regimes of this cryosphere region is of particular interest. This paper presents the results of Surface Energy Balance (SEB) study carried out in the upper Ganglass catchment in the Ladakh region of India, which feed directly to the River Indus. The point SEB is estimated using the one-dimensional mode of GEOtop model from 1 September 2015 to 31 August 2017 at 4727 m a.s.l elevation. The model is evaluated using field monitored snow depth variations (accumulation and melting), outgoing longwave radiation and one-year near-surface ground temperatures and showed good agreement with the respective simulated values. For the study period, the surface energy balance characteristics of the study site show that the net radiation (29.7 W m^{-2}) was the major component, followed by sensible heat flux (-15.6 W m^{-2}), latent heat flux (-11.2 W m^{-2}) and the ground heat flux was equal to -0.5 W m^{-2}. During both the years, the latent heat flux was highest in summer and lowest in winter, whereas the sensible heat flux was highest in post-winter and gradually decreased towards the pre-winter season. During the study period, snow cover builds up in the catchment initiated by the last week of December facilitating the ground cooling by almost three months (October to

Deleted: Cryosphere of t

Deleted: is unique with its

Deleted: cover

Deleted: its

Deleted: present

Deleted: ies

Deleted: radiation components,

Deleted: The study site have air temperature range of – 23.7 to 18.1 °C with a mean annual average temperature (MAAT) of -2.5°C and ground surface temperature range of -9.8 to 19.1 °C.

Deleted: with mean annual value of 28.9 W m^{-2}

Deleted: 13

Deleted: 5

Deleted: and

Deleted: 12

Deleted: 8

Deleted: , and t

Deleted: he

Deleted: 4

Deleted: The partitioning of energy balance components during the study period show that 47% of R_n was converted into H, 44% into LE, 1% into G and 7% for melting of seasonal snow.

Formatted: Font color: Auto

Formatted: Font color: Auto

Formatted: Font color: Auto

Formatted: Font color: Auto

Formatted: Font color: Auto

Deleted: Both the study years experienced distinctly different, low and high snow regime. Key differences due to this snow regime change in surface energy balance characteristics were observed during peak summer (July-August). The latent heat flux was higher (lower) during this period with 39 W m^{-2} (11 W m^{-2}) during high (low) snow years. Study also show that the sensible heat flux during the early summer season (May, June) of the high (low) snow was much smaller (higher) -3.4 W m^{-2} (36.1 W m^{-2}).

December) of sub-zero temperatures up to -20 °C providing a favourable environment for permafrost. It is observed that the Ladakh region have a very low relative humidity in the range of 43% as compared to, e.g., ~70% in the Alps facilitating lower incoming longwave radiation and strongly negative net longwave radiation averaging ~ -90 W m^{-2} compared to -40 W m^{-2} in the Alps. Hence, the high elevation cold-arid region land surfaces could be overall colder than the locations with more RH such as the Alps. Further, it is apprehended that high incoming shortwave radiation in the region during summer months may be facilitating enhanced cooling of wet valley bottom surfaces as a result of stronger evaporation.

Deleted: the Ladakh

Deleted:

Keywords: Cold-arid, Cryosphere, GEOtop, Himalaya, Leh, Permafrost, Surface Energy Balance

Deleted: , Permafrost

1 Introduction

The Himalayan cryosphere is essential for sustaining the flows in the major rivers originating from the region (Bolch et al., 2012, 2019; Hock et al., 2019; Immerzeel et al., 2012; Kaser et al., 2010; Lutz et al., 2014; Pritchard, 2019). These rivers flow through the most populous regions of the world (Pritchard, 2019) and insight on the processes driving the change is critical for evaluating the future trajectory of water resources of the area, ranging from small headwater catchments to large river systems (Lutz et al., 2014). It is hard to propose a uniform framework for the downstream response of these rivers as they originate and flow through various glacio-hydrological regimes of the Himalaya (Kaser et al., 2010; Thayyen and Gergan, 2010). Lack of understanding of multiple processes driving the cryospheric response of the region is limiting our ability to anticipate the subsequent changes and their impacts correctly. This has been highlighted by the recent studies which suggested the occurrence of higher precipitation in the accumulation zones of the glaciers than previously known (Bhutiyani, 1999; Immerzeel et al., 2015; Thayyen, 2020).

Deleted: important

Deleted: region

Deleted: is

Deleted: various

Deleted: ensuing

The sensitivity of mountain permafrost to climate change (Haeberli et al., 2010) leads to changes in permafrost conditions such as an increase in active layer thickness that eventually affect the ground stability (Gruber and Haeberli, 2007; Salzmann et al., 2007), trigger debris flows and rockfalls (Gruber et al., 2004; Gruber and Haeberli, 2007; Harris et al., 2001), hydrological changes (Woo et al., 2008), run-off patterns (Gao et al., 2018; Wang et al., 2017), water quality (Roberts et al., 2017), greenhouse gas emissions (Mu et al., 2018), alpine ecosystem changes (Wang et al., 2006), and unique construction requirements to negate the effects caused by ground-ice degradation (Bommer et al., 2010). These strongly affect the mountain communities and indicate the relevance of mountain permafrost on human livelihoods. Field observations suggest that ground-ice melt may be a critical water source in dry summer years in the cold-arid regions of Ladakh (Thayyen, 2015).

The energy balance at the earth's surface drives the spatio-temporal variability of ground temperature (Oke, 2002; Sellers, 1965; Westermann et al., 2009). It is linked to the atmospheric boundary layer, and location-dependent transfer mechanisms between land and the overlying atmosphere (Endrizzi, 2007; Martin and Lejeune, 1998; McBean and Miyake, 1972). The surface energy balance (SEB) in cold regions additionally depends on the seasonal snow cover, vegetation and moisture availability in the soil (Lunardini, 1981) and (semi-) arid areas exhibit their typical characteristics (Xia, 2010).

The role of permafrost is a key unknown variable in the Himalaya, especially in headwater catchments of the Indus basin. However, one can notice that the none of excellent studies about Himalayan cryosphere (e.g., Immerzeel et al., 2010; Lutz et al., 2014) discuss permafrost and its role in regional climate and Hydrology. And this is our prime motivation to take up the permafrost studies in the region. Recent studies have signalled significant permafrost area in the cold-arid upper Indus basin areas covering Ladakh (Wani et al., 2020). This study suggests the permafrost area in a small (15.4 km^2) catchment in the Ladakh region is 22 times of the

Moved (insertion) [7]

Deleted:

Deleted: another

Deleted:

Deleted: cover

Deleted: (Wani et al., 2019)

Deleted: cover

Deleted: ^{2})

glacier area. More coarse assessment in the Hindu Kush Himalaya (HKH) region suggests that the permafrost area extends up to 1 million km^2, which roughly translate into 14 times the area of glacier cover of the region (Gruber et al., 2017). Except for Bhutan, the expected permafrost areas in all other countries is larger than the glacier area. With two-thirds of the HKH underlain by permafrost, China has by far the largest estimated share (906x10^3 km^2) followed by India (40.1x10^3 km^2), Pakistan (26.6x10^3 km^2), Afghanistan (17.5x10^3 km^2), Nepal (11.1x10^3 km^2), Bhutan (1.2x10^3 km^2) and Myanmar (0.1x10^3 km^2) (cf. Table 1, Gruber et al., 2017). The mapping of rock glaciers using remote sensing suggested that the discontinuous permafrost in the HKH region can be found between 3500 m a.s.l. in Northern Afghanistan to 5500 m a.s.l. on the Tibetan Plateau (Schmid et al., 2015). Recently, Pandey (2019) published a remote sensing based rock glacier inventory of Himachal Himalaya and reports that the discontinuous permafrost can be found within an elevation range of 3000–5500 m a.s.l. Another rock glacier inventory from IHR suggests that the elevations above 4600 m a.s.l. are suitable for the occurrence of permafrost (Baral et al., 2019). Similarly, an initial localised estimate of 420 km^2 of permafrost is suggested in the Kullu district of Himachal Pradesh, India (Allen et al., 2016). The cold-arid region of Ladakh has reported sporadic occurrence of permafrost and associated landforms (Gruber et al., 2017; Wani et al., 2020) with the sorted patterned ground and other periglacial landforms such as ice-cored moraines. Previous studies of permafrost in the Ladakh region are from the Tso Kar basin (Rastogi and Narayan, 1999; Wünnemann et al., 2008), and the Changla region (Ali et al., 2018).

The SEB characteristics of different permafrost regions have been studied, e.g., the North American Arctic (Eugster et al., 2000; Lynch et al., 1999; Ohmura, 1982, 1984), European Arctic (Lloyd et al., 2001; Westermann et al., 2009), Tibetan Plateau (Gu et al., 2015; Hu et al., 2019; Yao et al., 2008, 2011, 2020), European Alps (Mittaz et al., 2000) or Siberia (Boike et al., 2008; Kodama et al., 2007; Langer et al., 2011a, 2011b). However, SEB studies of IHR

Deleted: cover

Deleted: two

Deleted: the first

Deleted: ,

Deleted: which falls in the Indian Himalayan Region (IHR). The inventory

Deleted: 3052

Deleted: 5503

Deleted: for Uttarakhand State, India

Formatted: Font color: Auto

Formatted: Font color: Auto

Deleted: the higher

Deleted: regions

Deleted:

Moved up [7]: Field observations suggest that ground-ice melt may be a critical water source in dry summer years in the cold-arid regions of Ladakh (Thayyen, 2015).

Deleted: a recent one from

Deleted: , where the depth of permafrost table was found to be ~110 cm

Deleted: The energy balance at the earth's surface drives the Spatio-temporal variability of ground temperature (Oke, 2002; Sellers, 1965; Westermann et al., 2009). It is linked to the atmospheric boundary layer, and location-dependent transfer mechanisms between land and the overlying atmosphere (Endrizzi, 2007; Martin and Lejeune, 1998; McBean and Miyake, 1972). The surface energy balance (SEB) in cold regions additionally depends on the seasonal snow cover, vegetation and moisture availability in the soil (Lunardini, 1981) and (semi-) arid areas exhibit their typical characteristics (Xia, 2010).

are limited, for example, the energy balance studies on glaciers by Azam et al. (2014) and Singh et al. (2020). The SEB also has a significant influence on regional and local climate (Eugster et al., 2000). During summer months, the permafrost creates a heat sink, which reduces the skin temperature, and therefore heat transfer to the atmosphere is also reduced (Eugster et al., 2000). This highlight that the knowledge of frozen ground and associated energy regimes are a critical knowledge gap in our understanding of the Himalayan cryospheric systems, especially in the Upper Indus Basin.

The goal of this manuscript is to improve the understanding of permafrost in cold-arid UIB areas and to advance our ability to analyse and simulate the characteristics of permafrost there. This can guide the application of available models in the Ladakh region which are calibrated (Boeckli et al., 2012) or validated (Cao et al., 2019; Fiddes et al., 2015) elsewhere. Furthermore, it can help to interpret differences in surface offset observed in Ladakh (Wani et al., 2020) and other permafrost areas (Boeckli et al., 2012; Hasler et al., 2015; PERMOS, 2019). Our working hypothesis is that the surface offset for particular terrain types in the UIB differs from what is known in other areas, driven by aridity and high elevation. We aim to improve the understanding of the SEB and its relationship with the ground temperature by working on three objectives: (1) Quantifying the SEB at South Pullu, as an exemplar for permafrost areas in the UIB. (2) Understand the pronounced seasonal and inter-annual variation of snowpack and GST, as these are intermediate phenomena between the SEB and permafrost. (3) Understanding key differences with other permafrost areas that have SEB observations.

2 Study area and data

2.1 Study area

The present study is carried out at South-Pullu (34.25°N, 77.62°E, 4727 m a.s.l.) in the upper Ganglass catchment (34.25°N to 34.30°N and 77.50°E to 77.65°E), Leh, Ladakh (Figure 1). Ladakh is a Union territory of India and has a unique climate, hydrology and landforms. Leh

Deleted: is very

Deleted: (

Deleted: ,

Deleted: ;

Deleted: ,

Deleted: key

Deleted: This study present SEB analysis of a permafrost environement in the cold-arid trans-Himalaya, where a recent study have identified significant permafrost cover (Wani et al., 2019). With this, we aim to provide a foundation for better understanding the micro-climatological drivers affecting permafrost distribution and temperature regimes in the area, to build hypotheses about similarities and major differences with other, better-investigated permafrost areas. This is important to guide the application of models calibrated (Boeckli et al., 2012) or tested (Cao et al., 2019; Fiddes et al., 2015) elsewhere for further investigations in the Ladakh region, where only little data on ground temperatures and permafrost are currently available. It will also help to interpret differences in the relationships of air and shallow ground temperatures (surface offset) observed in Ladakh (Wani et al., 2019) and other permafrost areas (Boeckli et al., 2012; Hasler et al., 2015; PERMOS, 2019). ¶
The specific objectives of this study are to (a) quantify the point Surface Energy Balance (SEB) and its components in a cold-arid Himalayan permafrost environment, (b) evaluate the quality of SEB assessment by modelling snow depth and near-surface ground temperature variations and compare with the field observations (c) understand the role of winter snowpack characteristics (timing, thickness and duration) and its effect on ground surface temperature, and (d) compare the SEB regime of cold-arid Himalaya with other better investigated permafrost regions of the world.

Deleted: in the Ladakh region

Deleted: at one point, based

Deleted: (4)

Formatted: Heading 1, Indent: Left: 0.75 cm is the district headquarter, where long-term climate data is available (Bhutiyani et al., 2007). Long-term mean precipitation of Leh (1908–2017, 3526 m a.s.l.) is 115 mm (Lone et al., 2019; Thayyen et al., 2013) and the daily minimum and maximum temperatures during the period (2010 to 2012) range between -23.4 to 33.8 °C (Thayyen and Dimri, 2014). The spatial area of the catchment is 15.4 km^2 and extends from 4700 m to 5700 m a.s.l. A small cirque glacier called as Phuche glacier with an area of 0.62 km^2 occupies the higher elevations of the catchment. A single stream flows through the valley of the catchment originating from Phuche glacier. This stream flows intermittently with most of the flow from May to October.

The catchment lies in the Ladakh mountain range and is part of the main Indus river basin. Geologically, the study catchment is part of the Ladakh batholith (Thakur, 1981). The study catchment also consists of steep mountain slopes with the valley bottom filled with glacio-fluvial deposits. Other sporadic landforms found in the catchment include patterned ground, boulder fields, peatlands, high elevation wetlands and a small lake. Many of these landforms point towards intense frost action in the area.

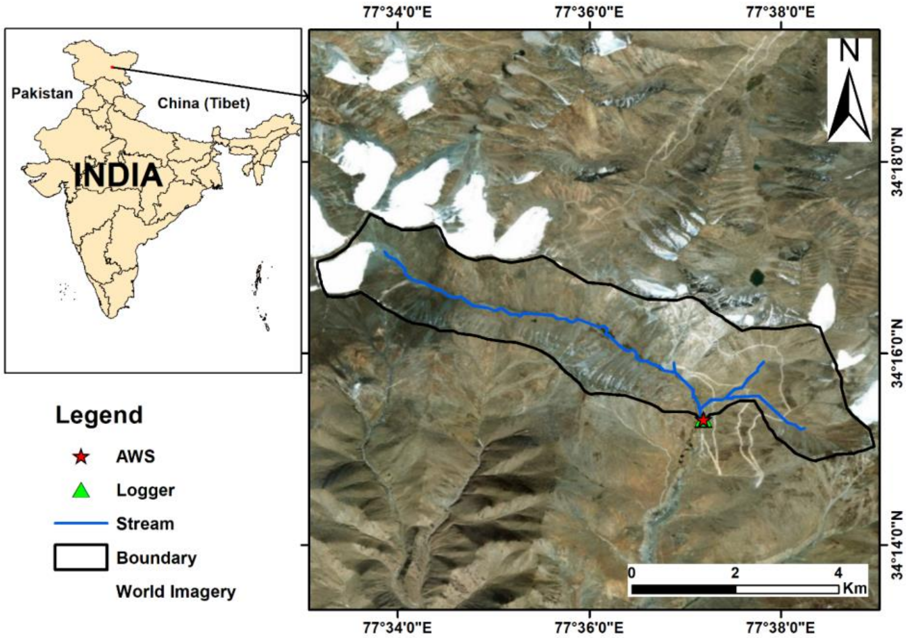

Figure 1 Location of the study site in the upper Ganglass catchment. (Base image sources on the right panel: © Esri, DigitalGlobe, GeoEye, Earthstar Geographic's, CNES/Airbus DS, USDA, USGS, AEX, Getmapping, Aerogrid, IGN, IGP, swisstopo, and the GIS User Community).

2.2 Meteorological data used

Moved (insertion) [2]

The automatic weather station (AWS) in the catchment is located at an elevation of 4727 m a.s.l. at South-Pullu (Figure 1). It is located in the wide deglaciated valley trending southeast. The site has a local slope angle of 15°, and the soil is sparsely vegetated. Weather data has been collected by a Sutron automatic weather station from 1 September 2015 to 31 August 2017. The study years 1 September 2015 to 31 August 2016 and 1 September 2016 to 31 August 2017 hereafter in the text will be designated as 2015-16 and 2016-17 respectively. The variables measured include air temperature, relative humidity, wind speed and direction, incoming and outgoing shortwave and longwave radiation and snow depth (Table 1). The snow depth is measured using a Campbell SR50 sonic ranging sensor with a nominal accuracy of ±1 cm (Table 1). To reduce the noise of the measured snow depth, a six-hour moving average is applied. Near-surface ground temperature (GST) is measured at a depth of 0.1 m near the AWS using miniature temperature data logger (MTD) manufactured by GeoPrecision GmbH, Germany. GST data was available only from 1 September 2016 to 31 August 2017 and is used for model evaluation, only. All the four solar radiation components, i.e., incoming shortwave (SW_{in}), outgoing shortwave (SW_{out}), incoming longwave (LW_{in}) and outgoing longwave (LW_{out}) radiation were measured. Before using these data in the SEB calculations, necessary corrections were applied (Nicholson et al., 2013; Oerlemans and Klok, 2002): (a) all the values of $SW_{in} < 5\ Wm^{-2}$ are set to zero, (b) when $SW_{out} > SW_{in}$ (3 % of data understudy), it indicates that the upward-looking sensor was covered with snow (Oerlemans and Klok, 2002). The SW_{out} can be higher than SW_{in} at high elevation sites such as this one due to high solar zenith angle during the morning and evening hours (Nicholson et al., 2013). In such cases, SW_{in} was corrected by SW_{out} divided by the accumulated albedo, calculated by the ratio of measured SW_{out} and measured SW_{in} for a 24h period (van den Broeke et al., 2004).

Deleted: The analysis of data was performed using R (R Core Team, 2016; Wickham, 2016, 2017; Wickham and Francois, 2016; Wilke, 2019). T

Deleted: ¶
¶
¶

Deleted: ¶

Table 1 Technical parameters of different sensors at South-Pullu (4727 m a.s.l.) in the upper Ganglass catchment, Leh. (MF: model forcing, ME: model evaluation).

Variable	Units	Sensor	Stated accuracy	Height (m)	Use
Air temperature	(°C)	Rotronics-5600-0316-1	±0.2 °C	2.2	MF
Relative humidity	(%)	Rotronics-5600-0316-1	±1.5%	2.2	MF
Wind speed	(m s^{-1})	RM Young 05103-45	±0.3 ms^{-1}	10	MF
Wind direction	(°)	RM Young 05103-45	±0.3°	10	MF
Incoming shortwave radiation	(W m^{-2})	Kipp and Zonen (CMP6) (285 to 2800nm)	±10%	4.6	MF
Outgoing shortwave radiation	(W m^{-2})	Kipp and Zonen (CMP6) (285 to 2800nm)	±10%	4.6	MF
Incoming longwave radiation	(W m^{-2})	Kipp and Zonen (CGR3) (4500 to 42000nm)	±10%	4.3	MF
Outgoing longwave radiation	(W m^{-2})	Kipp and Zonen (CGR3) (4500 to 42000nm)	±10%	4.3	ME
Snow depth	(m)	Campbell SR-50	±1cm	3.44	ME
Data logger	-	Sutron 9210-0000-2B	-	-	-
Near-surface ground temperature	(°C)	PT1000 in stainless steel cap (by GeoPrecision GmbH, Germany)	±0.1 °C	-0.1	ME

3 Methods

3.1 Estimation of precipitation from snow height

In high elevation and remote sites, the snowfall measurement is a difficult task with an under catch of 20–50% (Rasmussen et al., 2012; Yang et al., 1999). At the South Pullu station, daily precipitation including snow was measured using a non-recording rain gauge. In this high elevation area, an under catch of 23% of snowfall was reported earlier (Thayyen et al., 2015) [Unpublished work]. Here, we had the time resolution problem between total measured precipitation and other meteorological forcing's including SR50 snow depth (hourly and recorded by automatic weather station). Therefore, to match the temporal resolution of precipitation data with other meteorological forcing's, we adopted the method proposed by Mair et al. (2016), called Estimating SOlid and Liquid Precipitation (ESOLIP). This method

Deleted: ¶
¶

Moved (insertion) [3]

Deleted: /out

Deleted: /ME

Deleted: /out

Deleted: E

Deleted: platform

Deleted: EO

Formatted: Heading 1, Indent: Left: 0 cm, Hanging: 1 cm

Deleted: aterials and m

Deleted: ¶
Study area¶
The present study is carried out at South-Pullu (34.25°N, 77.62°E, 4727 m a.s.l.) in the upper Ganglass catchment (34.25°N to 34.30°N and 77.50°E to 77.65°E), Leh, Ladakh (Figure 1). Ladakh is a Union territory of India and has a unique climate, hydrology and landforms. Leh is the district headquarter, where long-term climate data is available (Bhutiyani et al., 2007). Long-term mean precipitation of Leh (1908–2017, 3526 m a.s.l.) is 115 mm (Lone et al., 2019; Thayyen et al., 2013) and the daily minimum and maximum temperatures during the period (2010 to 2012) range between -23.4 to 33.8 °C (Thayyen and Dimri, 2014). Due to scarce precipitation and warm summers, this part of the trans-Himalaya is classified as a cold-arid region characterised by strong land-atmosphere interactions, rarefied atmosphere and strong incoming solar radiation. The spatial area of the catchment is 15.4 km² and extends from 4700 m to 5700 m a.s.l. A small cirque glacier called as Phuche glacier with an area of 0.62 km² occupies the higher elevations of the catchment. A single stream flows through the valley of the catchment originating from Phuche glacier. This stream flows intermittently with most of the flow from May to October. ¶

Moved up [2]: Meteorological data used¶

Moved up [3]: Variable

Deleted: Variable

Deleted: (ESOLIP approach)

Deleted: It is a known fact that the snow water equivalent measurements in the mountainous region using collectors have significant errors due to under catch (Yang et al., 1999).

Deleted: T

Deleted: improve the data quality and makes use of snow depth and meteorological observations to estimate the sub-daily solid precipitation in terms of snow water equivalent (SWE). In ESOLIP, we considered liquid precipitation daily only.

The ESOLIP method consists of following steps: (a) filtering of precipitation readings: simple criteria based on relative humidity (RH) and global shortwave radiation was used such as, for an actual precipitation event, the RH > 50% and SWin < 400 W m^{-2}, (b) precipitation type determination: wet bulb temperature (T_w) is used to differentiate between rain and snow such as if T_w < 1 (SWE estimation) and if T_w >=1 (rain). The T_w is estimated by solving the psychrometric formula implicitly: $e = E(T_w) - \gamma(T_a - T_w)$, T_a is the air temperature, and e (hPa) is the vapour pressure in the air, E (hPa) is the saturation vapour pressure, and γ (hPa K^{-1}) is the psychrometer constant depending on air pressure, (c) estimation of density: the fresh snow density (ρ) was estimated based on air temperature (T_a) and wind speed (u) as below (Jordan et al., 1999):

$$\rho = 500 * [1 - 0.951 * exp(-1.4 * (278.15 - T_a)^{-1.15} - 0.008u_{10}^{1.7})], \qquad (1)$$

For 260.15 < T_a ≤ 275.65 K

$$\rho = 500 * [1 - 0.904 * \exp(-0.008u_{10}^{1.7})], \qquad (2)$$

For T_a ≤ 260.15 K

and (d) estimation of SWE ($SWE = h*\rho$): to estimate the SWE of single snowfall events using snow depth measurements, and identification of the snow height increments of the single snowfall events and an accurate estimate of the snow density are necessary.

3.2 Modelling of point surface energy balance

In this study, the open-source model GEOtop version 2.0 (hereafter GEOtop) (Endrizzi et al., 2014; Rigon et al., 2006) was used for the modelling of point surface energy balance including

Deleted: the winter precipitation. In this method,
Deleted: is estimated
Formatted: Superscript
Formatted: Font: Italic
Formatted: Font: Italic, Subscript
Formatted: Font: Italic
Formatted: Font: Italic, Subscript
Formatted: Font: Italic
Formatted: Font: Italic, Subscript
Formatted: Font: Italic
Formatted: Font: Italic, Subscript
Formatted: Font: Italic
Formatted: Font: Italic, Subscript
Formatted: Font: Italic
Formatted: Font: Italic
Formatted: Superscript
Formatted: Font: Italic
Formatted: Font: Italic, Subscript
Formatted: Font:
Formatted: Font: Italic
Formatted: Font: Italic, Subscript
Formatted: Font: Italic
Formatted: Font: Italic, Subscript
Formatted: Justified
Formatted: Font:
Deleted: 2.0

the evolution of the snow depth and the transfer of heat and water in snow and soil. GEOtop represents the combined ground heat and water balance, the exchange of energy with the atmosphere by taking into consideration the radiative and turbulent heat fluxes. The model has a multi-layer snowpack and solves the energy and water balance of the snow cover and soil including the highly non-linear interactions between the water and energy balance during soil freezing and thawing (Dall'Amico et al., 2011). It can be applied in complex terrain and makes it possible to account for topographical and other environmental variability (Fiddes et al., 2015; Gubler et al., 2013).

Previous studies have successfully applied GEOtop in mountain regions, e.g., simulating snow depth and ground temperature (Endrizzi et al., 2014), snow cover mapping (Dall'Amico et al., 2011b, 2018; Engel et al., 2017; Zanotti et al., 2004), ecohydrological processes (Bertoldi et al., 2010; Chiesa et al., 2014), modelling of ground temperature in complex topography (Fiddes and Gruber, 2012), water and energy fluxes (Hingerl et al., 2016; Rigon et al., 2006; Soltani et al., 2019), evapotranspiration (Mauder et al., 2018), permafrost distribution (Fiddes et al., 2015) or modelling ground temperatures (Bertoldi et al., 2010; Gubler et al., 2013).

Generally, the surface energy balance (SEB) (Eq. 3) is written as a combination of net radiation (R_n), sensible (H) and latent heat (LE) flux and heat conduction into the ground or to the snow (G) and must balance at all times (Oke, 2002):

$$R_n + H + LE + G - F_{surf} = 0 \quad (3)$$

where F_{surf} is the resulting latent heat flux in the snowpack due to melting or freezing, the sign convention adopted in this study is as, the energy fluxes towards the surface are positive, and negative if directed away from the surface (Mölg, 2004). During the summertime, when conditions for snow melting are prevailing at the ground surface, the F_{surf} is negative (loss from the system) as a result of energy available for melting snow and warming the ground under

Deleted: is a physically-based fully distributed model for modelling of water and energy balances at and below the soil surface. It

Deleted: also

Deleted: . Furthermore, the temporal evolution of snow depth and its effect on soil temperature are simulated. The GEOtop also simulates the

Field Code Changed

Deleted: ; Endrizzi et al., 2014

Deleted: The model solves Richard's equation in three or one dimensions, and the heat equation in one dimension (1D) (Endrizzi et al., 2014).

Deleted: high mountain regions with

Deleted: The model takes into account the effects of complex topography in the estimation of radiation components (Endrizzi et al., 2014), such as (i) the incoming solar radiation is partitioned into direct and diffuse components according to Erbs et al. (1982), (ii) taking into account the solar incidence angle and shadowing of direct incoming solar radiation by topography, (iii) the effects of topography on diffuse radiation coming on the surrounding terrain (Iqbal, 1983).

Deleted: The model can be operated in two configurations, either in pointwise (1D) or distributed mode (2D) and the processes of interest can be controlled through parameters (Endrizzi et al., 2014).

Deleted: s

Deleted: (Dall'Amico et al., 2018; Dall'Amico et al., 2011; Zanotti et al., 2004)

Deleted: processes

Deleted: In this study, only the energy fluxes over the snow cover and the ground surface in one-dimensional (1D) mode of GEOtop are used. ¶

Formatted: Highlight

Deleted: –

Deleted: –

Deleted: –

Deleted: F_{surf}

Deleted: energy flux at the surface.

Formatted: Subscript

snow free conditions. The positive F_{surf} (gain to the system) during summertime is the energy released to refreeze the water and represents the freezing flux.

In the cold regions, the SEB is a complex function of solar radiation, seasonal snow cover, vegetation, near-surface moisture content, and atmospheric temperature (Lunardini, 1981). Based on the in-situ available data, the calculation of SEB components like H, LE and G is difficult. For example, in the calculation of turbulent heat fluxes (H and LE), the wind speed and temperature measurements near the ground surface are required at two heights, which are generally not available. Therefore, parameterisation method like bulk aerodynamic method is used which is valid under statically neutral conditions in the surface layer (Stull, 1988). Hence, application of a tested model like GEOtop (Endrizzi et al., 2014; Rigon et al., 2006) is a good alternative for the estimation of these fluxes. However, in the GEOtop (Endrizzi et al., 2014), the general equation of SEB (Eq. 3) is linked with the water balance and is written as (Eq. 4): In GEOtop, the surface heat flux (F_{surf}) is the energy available for exchange and is given by the sum of net shortwave (SW_n) and net longwave (LW_n) radiations and turbulent heat fluxes, i.e. sensible (H) and latent heat flux (LE). The surface heat flux equation (Eq.):

$$F_{surf}(T_s) = SW_n + LW_n(T_s) + H(T_s) + LE(T_s, \theta_w) \qquad (4)$$

where T_s, the temperature of the surface, is an unknown in the equation, SW_n is the shortwave radiation, LW_n is the net longwave radiation. The F_{surf} is a function of the T_s. Other terms in Eq. 4 which are a function of T_s include LW_n, H and LE. In addition, the LE also depends on the soil moisture at the surface (θ_w), linking the SEB and water balance equations. The equations and the key elements of GEOtop are explained in Endrizzi et al. (2014), and here, only a brief description of the equations that are of interest in this study is given. The SW_n in Eq. 4 is equal to the difference between the incoming solar radiation (SW_{in}) coming from the atmosphere and the reflected shortwave radiation (SW_{out}) (Oke, 2002).

Formatted: Subscript

Formatted: Subscript

Deleted: During summer time when the melting conditions prevail, the F_{surf} is positive and is the energy available for melting snow, otherwise, F_{surf} is equal to zero.¶ But

Deleted: s

Deleted: are

Deleted: described separately

Deleted: .

Moved down [1]: The equations and the key elements of GEOtop are explained in Endrizzi et al. (2014), and here, only a brief description of the equations that are of interest in this study is given.

Formatted: Font color: Red

Formatted: Font color: Red

Deleted: Q

Formatted: Font color: Red

Formatted: Font color: Red

Formatted: Font color: Red

Formatted: Font color: Red

Formatted: Font color: Red

Formatted: Font color: Red

Formatted: Font color: Red

Formatted: Font color: Red

Formatted: Font color: Red

Commented [J1]: Delete in final version as the deletion of these line is creating problem in saving the document.

Deleted: 4

Deleted: used in GEOtop is given below

Deleted: Q

Deleted: –

Deleted: –

Deleted: 4

Deleted: Q_s

Deleted: temperature at the surface (

Deleted:), which is an unknown in the equation

Deleted: 4

Deleted: In Eq. 4, the sum of SW_n and LW_n is equal to the net radiation (R_n) (Oke, 2002). The sign convention adopted is as, energy is considered as gain for the surface or system, if R_n is positive and negative for H and LE. Conversly, energ ...

Moved (insertion) [1]

Deleted: ¶

Deleted: term

Deleted: The SW_{out} is given by SW_{in} multiplied by the ...

Also, LW_n in Eq. 4 is equal to the difference between the incoming longwave radiation (LW_{in}) coming from the atmosphere and the outgoing longwave radiation (LW_{out}) radiated by the surface (Oke, 2002).

The LW_{out} radiated by the surface is also estimated using the Stefan-Boltzmann law (Eq. 5), as below:

$$LW_{out} = \epsilon_s . \sigma . T_s^4 \qquad (5)$$

where T_s is the surface temperature (K) and ϵ_s is the surface emissivity.

The turbulent fluxes (H and LE) are driven by the gradients of temperature and specific humidity between the air and the surface, and due to turbulence caused by winds as primary transfer mechanism in the boundary layer (Endrizzi, 2007). GEOtop estimates the turbulent heat fluxes H (Eq. 6) and LE (Eq. 7) using the flux-gradient relationship (Brutsaert, 1975; Garratt, 1994) as below:

$$H = \rho_a c_p w_s \frac{T_a - T_s}{r_a} \qquad (6)$$

$$LE = \beta_{YP} L_e \rho_a c_p w_s \frac{Q_a - \alpha_{YP} Q_s^*}{r_a} \qquad (7)$$

where ρ_a is the air density (kg m^{-3}), w_s is the wind speed (m s^{-1}), c_p the specific heat at constant pressure (J kg^{-1} K^{-1}), L_e the specific heat of vaporisation (J kg^{-1}), Q_a and Q_s^* are the specific humidity of the air (kg kg^{-1}) and saturated specific humidity at the surface (kg kg^{-1}) respectively, and r_a is the aerodynamic resistance (-). The aerodynamic resistance is obtained applying the Monin–Obukhov similarity theory (Monin and Obukhov, 1954), which requires that values of wind speed, air temperature and specific humidity are available at least at two different heights above the surface. But the values of these variables are generally measured at standard height above the surface and can be used for near surface with following assumptions:

Deleted: 8

Formatted: Font:

Deleted: 8

Deleted: main

Deleted: 9

Deleted: 10

Deleted: 9

Deleted: 10

Moved (insertion) [4]

Deleted: al

Deleted: and available at only one

Deleted: are sufficient only based on

Deleted:

Deleted: just above the surface

(a) the air temperature is equal to the ground surface temperature; however, this assumption leads to the boundary condition nonlinearity, (b) the specific humidity is equal to $\alpha_{YP} Q_s^*$, and (c) wind speed is equal to zero.

The β_{YP} and α_{YP} are the coefficients (Eq. 8 and 9) that take into account the soil resistance to evaporation, and only depend on the liquid water pressure close to the soil surface. They are calculated according to the parameterisation of Ye and Pielke (1993), which considers evaporation as the sum of the proper evaporation from the surface and diffusion of water vapour in soil pores at greater depths:

$$\beta_{YP} = \chi_p(g) - \frac{[\chi_p(g) - \theta_g]}{1 + \frac{\chi_p(1) - \theta_{(1)}}{\chi_p(g) - \theta_g} \frac{r_a}{r_d}} \quad (8)$$

$$\alpha_{YP} = \frac{1}{\beta_{YP}} \left[\theta_g + \frac{\chi_p(1) - \theta_{(1)}}{1 + \frac{\chi_p(1) - \theta_{(1)}}{\chi_p(g) - \theta_g} \frac{r_a}{r_d}} \frac{r_a}{r_d} h_{s(\theta_1)} \frac{q^{sat}_{(Ts1)}}{q^{sat}_{(Tg)}} \right] \quad (9)$$

q^{sat} is the specific humidity in the saturated condition, the subscripts g and 1 in above two equations refer to the ground surface and a thin layer next to the ground surface, respectively, θ is the volumetric water content of the soil, χ_p is the volumetric fraction of soil pores, h_s is the relative humidity in the pores, T_g is the temperature at the ground surface, r_d is the soil resistance to water vapour diffusion.

3.2.1 The heat equation and snow depth

The equation (Eq. 10) representing the energy balance in a soil volume subject to phase change in GEOtop is given below (Endrizzi et al., 2014):

$$\frac{\partial U^{\text{ph}}}{\partial t} + \nabla.\mathbf{G} + S_{en} - \rho_w \left[L_f + c_w \left(T - T_{ref} \right) \right] S_w = 0 \qquad (10)$$

where U^{ph} is the volumetric internal energy of soil (J m^{-3}) subject to phase change, t(s) time, $\nabla\cdot$ the divergence operator, G the heat conduction flux (W m^{-2}), S_{en} is the energy sink term

Deleted: .

Moved up [4]: The aerodynamical resistance is obtained applying the Monin–Obukhov similarity theory (Monin and Obukhov, 1954), which requires that values of wind speed, air temperature and specific humidity are available at least at two different heights above the surface.

Formatted: Font: Not Bold

Formatted: Centered

Formatted: Centered

Formatted: Font: Not Bold

Formatted: Font: Italic

Formatted: Font: Italic

Formatted: Font: Italic, Subscript

Formatted: Font: Italic

Formatted: Font: Italic, Subscript

Formatted: Font: Italic

Formatted: Font: Italic, Subscript

Deleted: The input meteorological data required for running the 1D GEOtop model include time series of precipitation, air temperature, relative humidity, wind speed, wind direction and solar radiation components and the description of the topography (slope angle, elevation, aspect angle, and sky view factor) for the simulation point. Also, the latitude and longitude of the study area have to be defined to allow the model to calculate the solar zenith angle, which is important for shadowing estimations.¶
H

Moved (insertion) [5]

Deleted: 1

Deleted: :(Endrizzi et al., 2014)

Deleted:

Moved up [5]: (Eq. 11):

Deleted: 11

(W m^{-3}), S_w is the mass sink term (s^{-1}), L_f (J kg^{-1}) the latent heat of fusion, ρ_w the density of liquid water in soil (kg m^{-3}), c_w is the specific thermal capacity of water (J kg^{-1} K^{-1}), T (°C) the soil temperature and T_{ref} (°C) the reference temperature at which the internal energy is calculated. If G is written according to Fourier's law, the Eq. 10 becomes:

$$\frac{\partial U^{\mathrm{ph}}}{\partial t} + \nabla.(\lambda_T \nabla \mathrm{T}) + S_{en} - \rho_w\left[L_f + c_{\mathrm{w}}\left(T - T_{ref}\right)\right]S_w = 0 \qquad (11)$$

where λ_T is the thermal conductivity (W m^{-1} K^{-1}). The λ_T being a non-linear function of temperature, because the proportion of liquid water and ice contents depends on temperature. For the calculation of λ_T, the GEOtop uses the method proposed by Cosenza et al. (2003). The detailed description of the heat conduction equation used in GEOtop can be found in Endrizzi et al. (2014).

The snow cover buffers the energy exchange between the soil and atmosphere and critically influences the soil thermal regime (Endrizzi et al., 2014). GEOtop includes a multi-layer, energy-based, Eulerian snow modelling approach. In GEOtop, the equations for snow modelling are similar to the ones used for the soil matrix (Endrizzi et al., 2014). The discretisation of snow in GEOtop is done to describe the thermal gradients which are finer near the surface (with the atmosphere) and at the bottom (with soil). In GEOtop, the effective thermal conductivity at the interface of snow and ground is calculated similarly as in between different soil layers using the method of Cosenza et al. (2003). In GEOtop, the fresh snow density is computed using the Jordan et al. (1999) formula, which is based on air temperature and wind speed. More details about the snow metamorphism compaction rates and the snow discretisation in GEOtop can be found in the appendix D2 and D3, respectively of (Endrizzi et al., 2014).

Formatted: Font: Not Bold

Formatted: Superscript

Formatted: Superscript

Deleted: (

Deleted: ,

Deleted: (

Deleted: ,

3.2.2 Model setup and forcing’s

The 1D GEOtop simulation was carried out at South-Pullu (Figure 1). The soil column is 10 m deep and is discretised into 19 layers, with thickness increasing from the surface to the deeper layers. The top 8 layers close to the ground surface were resolved with thicknesses ranging from 0.1 to 1 m, because of the higher temperature and water pressure gradients near the surface (Endrizzi et al., 2014), while the lowest layer is 4.0 m thick.

The snowpack is discretised in 10 layers, which are finer at the top at the interface with the atmosphere and the bottom with the soil.

The model was initialised at a uniform soil temperature of -0.5 ºC and spun up by repeatedly modelling the soil temperature down to 1 m (2 years*25 times), and then using the modelled soil temperatures as an initial condition to repeatedly simulate soil temperature down to 10 m (2 years *25 times) (c.f., Fiddes et al., 2015; Gubler et al., 2013; Pogliotti, 2011). Preliminary tests show that the minimum number of repetitions required to bring the soil column to equilibrium was 25 (Figure *S1*). The values of all the input parameters used is given in Appendix (Table A1 to A4) in the supplementary material.

The input meteorological data required for running the 1D GEOtop model include time series of precipitation, air temperature, relative humidity, wind speed, wind direction and solar radiation components and the description of the site (slope angle, elevation, aspect angle, and sky view factor) for the simulation point. The model was run at an hourly time step corresponding to the measurement time step of the meteorological data.

3.3 Model performance evaluation

While the accuracy of simulated energy fluxes cannot be quantified, the quality of GEOtop simulations is evaluated based on proxy variables such as snow depth, GST and the LW_{out}. These variables were chosen because they have not been used to drive the model, and they represent different physical processes affected by surface energy balance. For example, (a) the

Deleted: <#>Modelling of snow depth¶
<#>The snow cover buffers the energy exchange between the soil and atmosphere and critically influences the soil thermal regime. In GEOtop, the equations for snow modelling are similar to the ones used for the soil matrix (Endrizzi et al., 2014). The snow processes are solved in a particular order such as (i) solving the heat equation for snow, (ii) metamorphism of the snowpack, (iii) water percolation in the snow and (iv) accumulation due to snow precipitation (Endrizzi et al., 2014). ¶

Deleted: <#> and forcing

Deleted: than in the middle

Deleted: At the top and bottom regions of the snowpack, the vertical gradients are high because of the interactions with the atmosphere at top and the soil at the bottom (Endrizzi et al., 2014).

Deleted: . The soil column in the model is 10 m deep. The model is initialised by

Deleted: = 50 years

Deleted: 50

Deleted: years

Deleted:

Deleted: and finally simulating soil temperatures down to 10 m depth. This initialisation technique has been successfully applied in earlier work

Field Code Changed

Deleted: In this study, the data recorded by the AWS was used as model forcing, and the forcing data consist of hourly air temperature, wind speed and direction, and global incoming shortwave radiation. The ESOLIP estimated hourly precipitation was also used as forcing to the model.

Deleted: s

Deleted: The evaluation of point SEB was done

Deleted: three variables such as radiation components,

Deleted: and the

Formatted: Subscript

Deleted: influencing

Deleted: the

Deleted: at the ground

Deleted: , (a) the radiation components are the main input driving the surface energy balance,

Deleted: b

melt-out date of the snow depth is a good indicator showing how good the surface mass and energy balance is simulated, and (b) the GST is the result of all the processes occurring at the ground surface such as radiation, turbulence, latent and sensible heat fluxes (Gubler, 2013), and (c) LW_{out} which is governed by the temperature and emissivity at the surface and the Eq. 3 is solved in terms of skin temperature. Therefore, the LW_{out} is used as a proxy for the evaluation of SEB.

Model performance is evaluated based on the measured and the simulated time series (Gubler et al., 2012). Typically, a variety of statistical measures are used to assess the model performance because no single measure encloses all aspects of interest. In this study also, R^2 (Carslaw and Ropkins, 2012), mean bias difference (MBD) and the root mean square difference (RMSD) (Badescu et al., 2012; Gubler et al., 2012; Gueymard, 2012), MB and RMSE (Gupta et al., 1999), and NSE (Nash and Sutcliffe, 1970) were used (Eq. *S*1 to *S*6).

4 Results

4.1 Model evaluation

In this section, the capability of GEOtop to reproduce the proxy variables is evaluated. The model was evaluated based on snow depth, one-year GST and the LW_{out}. In this study, the simulation results are based on the standard model parameters obtained from the literature (Table 2 and 3, Gubler et al., 2013) and were not improved by trial and error and the same simulation results are used for model evaluation.

4.1.1 Evaluation of snowpack

Snow depth variations simulated by GEOtop are compared with observations from 1 September 2015 to 31 August 2017 (Figure 2). The model captures the peaks, start and melt-out dates of the snowpack, as well as overall fluctuations (R^2 = 0.98, RMSE = 59.5 mm, MB = 16.7 mm, NSE = 0.91, Instrument error = ±10 mm) (Figure *S*2). The maximum standing snow height (*h*) simulated by the GEOtop was 1219 mm in comparison to the 1020 mm measured in

Deleted: c

Formatted: Subscript

Formatted: Subscript

Deleted: evaluate

Deleted: enclose

Deleted: different model evaluation statistics were used for

Formatted: Superscript

Formatted: Font: Italic

Formatted: Font: Italic

Deleted: (

Deleted: a) radiation components, and (b) GST and the snow depth as described below.

Deleted: <#>**Performance statistics for evaluation of radiation components**¶
<#>For the evaluation of radiation components, we prefer the statistics mean bias difference (MBD) and the root mean square difference (RMSD) (Badescu et al., 2012; Gubler et al., 2012; Gueymard, 2012). These statistics indicate model prediction accuracy (Stow et al., 2003). The MBD (Eq. 12) is a simple and familiar measure that neglects the magnitude of the errors (i.e. positive errors can compensate for negative ones) (Gubler et al., 2012):¶
<#>¶ ...

Formatted: Subscript

Formatted: Not Highlight

Formatted: Font: Italic

Formatted: Font: Italic

Deleted:

the field. In the low snow year, the maximum simulated *h* was 326 mm in comparison to the 280 mm measured in the field. During the melting period of the low and high snow years, the snow depth was slightly under-estimated. However, during the accumulation period of high snow year (2016-17), the *h* was rather overestimated by the model.

Formatted: Font: Italic

Formatted: Font: Italic

Furthermore, the performance of the ESOLIP estimated precipitation was evaluated against a controlled run with precipitation data measured in the field (Figure 2). ESOLIP is the superior approach for precipitation estimation, where snow depth and necessary meteorological measurements are available.

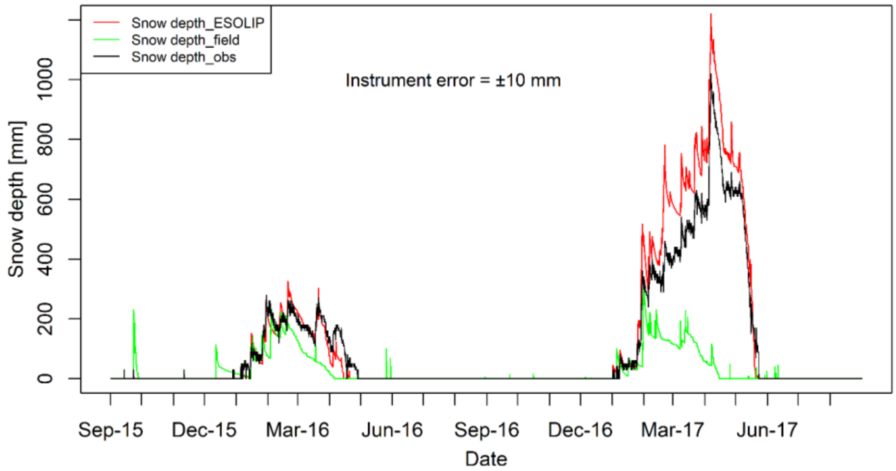

Figure 2 Comparison of hourly observed and GEOtop simulated snow depth at South-Pullu (4727 m a.s.l.) from 1 September 2015 to 31 August 2017. The black line denotes the snow depth measured in the field by SR50 sensor. The red (Snow depth_ESOLIP) and green (Snow depth_field) lines in the plot indicate the GEOtop simulated snow depth based on ESOLIP estimated precipitation and precipitation measured in the field, respectively.

4.1.2 Evaluation of near-surface ground temperatures (GST)

GST is simulated (GST_sim) on an hourly basis and compared with the observed values (GST_obs) near the AWS, available from 1 September 2016 to 31 August 2017 (Figure 3). The

Formatted: Space After: 0 pt

results show a reasonably good linear agreement between the simulated and observed GSTs (Figure *S3*, R^2 = 0.97, MB = -0.11 °C, RMSE = 1.63 °C, NSE = 0.95, Instrument error = ±0.1 °C). The model estimated the dampening of soil temperature fluctuations by the snowpack and the zero-curtain period at the end of melt-out of the snowpack reasonably well.

Deleted: reasonably well

Deleted: ;

Formatted: Not Highlight

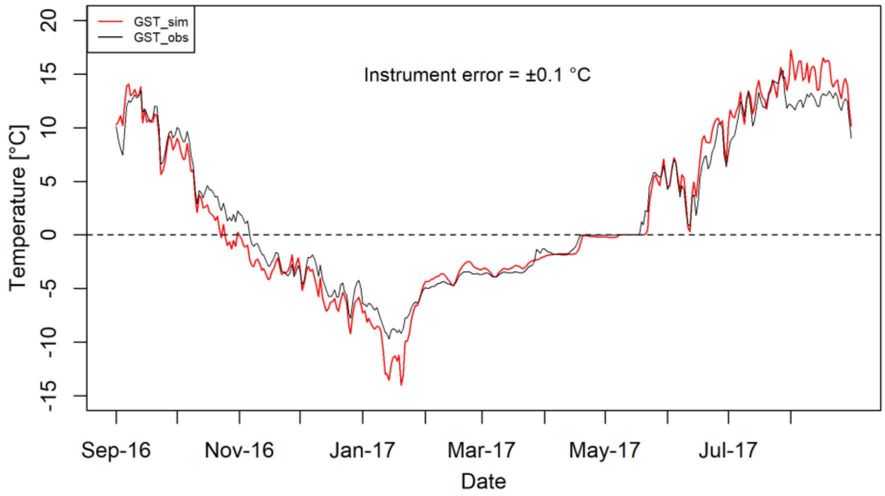

Figure 3 Comparison of daily mean observed (GST_obs, °C) and GEOtop simulated near-surface ground temperature (GST_sim, °C) at South-Pullu (4727 m a.s.l.) from 1 September 2016 to 31 August 2017.

Formatted: Caption

4.1.3 Evaluation of outgoing longwave radiation

Formatted: Font: Bold

Modelled LW_{out} is evaluated with the observed measurements and a comparison of daily mean observed, and simulated LW_{out} is shown in Figure 4. The daily mean LW_{out} matches very well with the observed data, except during summer months when the simulated LW_{out} was slightly overestimated than the observed values. The hourly LW_{out} shows a good linear relationship (Figure *S4*, R^2 = 0.93, NSE = 0.73) but the GEOtop slightly overestimates the LW_{out} (MBD = 3 %) with RMSD value of 10 % (Instrument error = ±10%).

Formatted: Normal, Justified

Formatted: Subscript

Formatted: Subscript

Formatted: Subscript

Formatted: Subscript

Based on the evaluation of LW_{out}, the GEOtop can simulate the surface temperature at the point scale; therefore, we believe that it can reasonably calculate the SEB components.

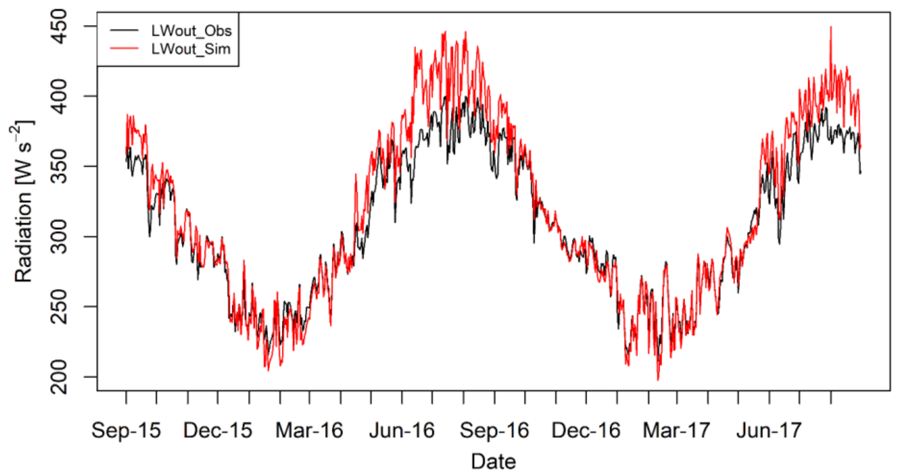

Figure 4 Comparison of daily mean observed outgoing longwave radiation (LW_{out}_obs) and GEOtop simulated (LW_{out}_sim) at South-Pullu (4727 m a.s.l.) from 1 September 2015 to 31 August 2017. The instrument error for the Kipp and Zonen (CGR3) (4500 to 42000nm) radiometer is ±10%.

4.2 Meteorological characteristics

The range of the meteorological variables measured at South-Pullu (4727 m a.s.l.) study site is given in Table 2 to provide an overview of the prevailing weather in the study region. The daily mean air temperature (T_a) throughout the study period varies between -19.5 to 13.1 °C with a mean annual average temperature (MAAT) of -2.5 °C (Figure 5A). The T_a shows significant seasonal variations and instantaneous hourly temperature at the study site range between -23.7 °C in January and 18.1 °C in July. During the two-year study period, sub-zero mean monthly temperature prevailed for seven months from October to April in both the years (2015-16 and 2016-17). The monthly mean T_a during pre-winter months (September to December) of 2015-16 and 2016-17 was −4.6 and -2.7 °C respectively. During the core winter months (January to

Formatted: Not Highlight
Formatted: Subscript, Not Highlight
Formatted: Not Highlight
Formatted: Not Highlight
Formatted: Not Highlight
Formatted: Not Highlight
Formatted: Normal
Formatted: Normal, Justified
Formatted: Subscript
Formatted: Subscript
Deleted: ¶
Deleted: A summary
Deleted: conditions
Deleted: 2A
Deleted: two year

February) of 2015-16 and 2016-17, the respective monthly mean T_a was -13.1 and -13.7 °C, for post-winter months (March and April), mean monthly T_a was -5.8 and -8 °C, respectively. For summer months (May to August), the respective monthly mean T_a was 6.6 and 5.5 °C. A sudden change in the mean monthly T_a characterises the onset of a new season, and the most evident inter-season change was found between the winter and summer with a difference of about 16 °C during both the years.

The mean daily GST recorded by the logger near the AWS available for one year (1 September 2016 to 31 August 2017) is also plotted along with air temperature (Figure 5A). The mean daily GST ranges from -9.7 to 15.4 °C with mean annual GST of 2.1 °C. The instantaneous hourly GST at the study site range between -10.7 °C in December and 20.2 °C in July. The GST followed the pattern of air temperature, but during winter, the snow cover dampened the pattern. The GST was higher than the T_a except for a short period during snowmelt. The snow depth shown in Figure 5A is described in sub-section 4.3.

Mean relative humidity (RH) was equal to 43% during the study period (Figure 5B). The daily average wind speed (u) ranges between 0.6 (29 January 2017) to 7.1 m s^{-1} (6 April 2017) with a mean wind speed of 3.1 m s^{-1} (Figure 5C). The instantaneous hourly u was plotted as a function of wind direction (WD) (Figure *S5*) for the study period which shows that there is a persistent dominance of katabatic and anabatic winds at the study site, which is typical of a mountain environment. The average WD during the study period was southeast (148°) (Figure 5D).

Deleted: and f

Deleted: 2A

Deleted: 1

Deleted: 1

Deleted: 9.8

Deleted: 19

Deleted: 1

Formatted: Justified, Space After: 0 pt, Line spacing: Double

Deleted: 2B

Deleted: The instantaneous hourly values of RH at the study site range between 3% (1 October 2016) and 100% (22 September 2015). The daily mean RH greater than 50% and 80% was recorded on 224 and 18 days respectively. The average RH during the pre-winter months (September to December) of the 2015-16 year was greater (39%) in comparison to RH (28%) recorded during pre-winter months of the 2016-17 year. However, during core winter months (January to February) of the 2015-16 year was smaller (42%) in comparison to the RH (53%) recorded during core winter months of the 2016-17 year. The average RH during the summer months (May to August) of the 2015-16 year was smaller (45%) in comparison to RH (51%) recorded during summer months of the 2016-17 year. Furthermore, for the low snow year (2015-16), the annual mean RH was 42.7%, and for the high snow year (2016-17) the annual mean RH was 44%. ¶

Deleted: 2C

Deleted: The hourly maximum instantaneous value of u recorded was 11.1 m s^{-1} (4 February 2017). The annual average u was 3.2 and 2.9 m s^{-1} during the years 2015-16 and 2016-17 respectively.

Deleted: *S2*

Deleted: 2D

Deleted: ¶

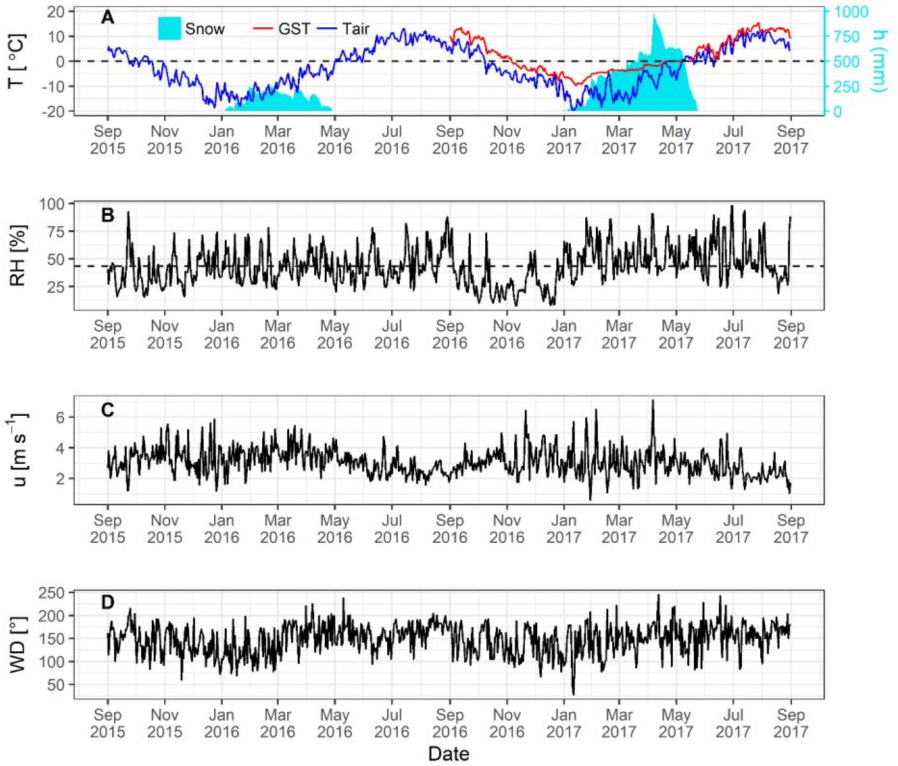

Figure 5 Daily mean values of observed (A) air temperature (blue) and one-year GST (red) (T, °C), snow depth (mm) on the secondary axis; (B) relative humidity (RH, %) with a dashed line as mean RH; (C) wind speed (u, ms^{-1}); and (D) wind direction (WD, °); at South-Pullu (4727 m a.s.l.) in the upper Ganglass catchment, Leh from 1 September 2015 to 31 August 2017.

The daily measured total precipitation at the study site equals 97.8 and 153.4 mm w.e. during the years 2015–16 and 2016–17 respectively. After adding 23% under catch (Thayyen et al., 2015) [unpublished work] to the total snow measurements, the total precipitation amount equal to 120.3 and 190.6 mm w.e. for the years 2015–16 and 2016–17 respectively. During the study period, the observed highest single-day precipitation was 20 mm w.e. recorded on 23 September 2015 and the total number of precipitation days were limited to 63. The snowfall

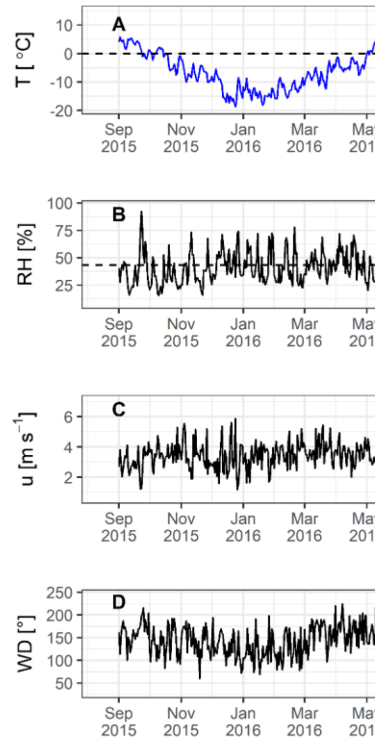

Deleted:

Deleted: 2

Deleted: Ta,

occurs mostly during the winter period (December to March) with some years witnessing extended intermittent snowfall till mid-June, as experienced in this study during the year 2016-17.

The precipitation estimated by the ESOLIP approach at the study site equals 92.2 and 292.5 mm w.e. during the years 2015–16 and 2016–17 respectively. The comparison between observed precipitation (mm w.e.) and the one estimated by the ESOLIP approach is given in (Table *S1*). In Table *S1*, the difference between the observed precipitation (mm w.e.) and the one estimated by the ESOLIP approach is mainly due to the under-catch of winter snow recorded by the Ordinary Rain Gauge.

4.3 Observed radiation components and snow depth

The observed daily mean variability of different components of radiation, albedo and snow depth from 1 September 2015 to 31 August 2017 at South-Pullu (4727 m a.s.l.) is shown in Figure 6. Daily mean SW_{in} varies between 24 and 378 W m^{-2} (Table 2). Highest hourly instantaneous short wave radiation recorded during the study period was 1358 W m^{-2}. Such high values of SW_{in} are typical of a high elevation arid-catchment (e.g., MacDonell et al., 2013). Persistent snow cover during the peak winter period for both the years extending from January to March resulted in a strong reflection of SW_{in} radiation (Figure 6A). During most of the non-snow period, mean daily SW_{out} radiation (Figure 6A) remain more or less stable below 100 W m^{-2}. Daily mean SW_{out} varies between 2.4 and 262.6 W m^{-2} with a mean value of 83.3 W m^{-2} (Table 2). The daily mean LW_{in} shows high variations and ranges between 109 and 345 W m^{-2} with an average of 220 W m^{-2} (Figure 3B, Table 2). Whereas LW_{out} was relatively stable and varied between 211 and 400 W m^{-2} with an average of 308 W m^{-2} (Figure 6B, Table 2). The LW_{out} shows higher daily fluctuations during the summer months as compared to the core winter months. The daily mean SW_n during the study period ranges between 2.5 and 319 W m^{-2} with a mean value of 127 W m^{-2}. The SW_n follows the pattern of SW_{in}, and for both the years,

Deleted: June,as

Formatted: Font: Italic

Deleted: 3

Deleted: 3A

Deleted: free

Deleted: 3A

Deleted: 3B

during the wintertime, the SW_n was close to zero due to the high reflectivity of snow (Figure 3C). The daily mean LW_n varies between -163 and 17 W m^{-2}. The LW_n does not show any seasonality and remain more or less constant with a mean value of -88 W m^{-2} (Figure 6C). The mean daily observed R_n ranges from -80.5 to 227.1 W m^{-2} with a mean of 39.4 W m^{-2} (Table 2). During both the years 2015–16 and 2016–17, the R_n was high in summer and autumn but low in winter and spring. From January to early April (2015–16) and January to early May (2016–17), when the surface was covered with seasonal snow, the R_n rapidly declined to low values, or even became negative (Figure 6D). Albedo (α) is calculated as the ratio of daily mean SW_{out} to daily mean SW_{in}. The α is of particular importance in the SEB and in the Earth's radiation balance that dictates the rate of heating of the land surface under different environmental conditions (Strugnell and Lucht, 2001). The daily mean observed α at the study site ranges from 0.04 to 0.95, with a daily mean value of 0.43 (Table 2). However, the value of broadband albedo is not greater than 0.85 (Roesch et al., 2002), and the maximum value (0.95) recorded at the study site might be due to the instrumental error. The daily mean α was low in summer and high in winter and increased significantly when the ground surface was covered with snow (Figure 6E).

Both the years (2015–16 and 2016–17) experienced contrasting snow cover characteristics during the study period (Figure 6F). The year 2015-16 experienced low snow as compared to 2016-17. During the 2015-16 year, the snowpack had a maximum depth of 258 mm on 30 January 2016, whereas, during the 2016-17 year, the maximum was 991 mm on 07 April 2017. The snow cover duration was 120 days during low snow year (2015-16) and 142 days during the high snow year (2016–17). The site became snow-free on 27 April in 2016 and on 23 May in 2017. Higher elevations of the catchment become snow-free around 15 July in 2016 while the snow cover at glacier elevations persisted till 22 August in 2017. For both the year's snow

Deleted: with higher values during summertime and low values and relatively stable during winter

Formatted: Subscript

Deleted: 3C

Deleted: When

Deleted: surface was covered with the thick snow during January to early April in 2015–16 and during January to early May in 2016–17,

Deleted: values

Deleted: 3D

Deleted: and

Deleted: is

Deleted: 1

Deleted: 48

Deleted: 2

Deleted: 3E

Formatted: Normal, Justified

Deleted: 3F

cover at lower elevations initiated by the end of December and the catchment experienced sub-zero mean monthly temperatures since October.

Table 2 Two year range of observed daily mean radiation components (SW_{in}, SW_{out}, LW_{in} and LW_{out}, SW_n, LW_n), surface albedo (α), net shortwave and longwave radiation (SW_n and LW_n), air temperature (T_a), wind speed (*u*), relative humidity (RH), precipitation (P), and snow depth (h) for the study period (1 September 2015 to 31 August 2017) at South-Pullu (4727 m a.s.l.).

Variable	Units	Min.	Max.	Mean
SW_{in}	W m^{-2}	24.1	377.8	210.4
SW_{out}	W m^{-2}	(-)2.4	(-)262.6	(-)83.4
α	-	0.04	0.95	0.43
LW_{in}	W m^{-2}	109.0	344.7	220.4
LW_{out}	W m^{-2}	(-)211.3	(-)400.0	(-)308.0
SW_n	W m^{-2}	2.5	318.7	127.0
LW_n	W m^{-2}	-163	17.1	-87.6
T_a	°C	-19.5	13.1	-2.5
u	m s^{-1}	0.6	7.1	3.1
RH	%	8	98	43.3
P	mm w.e	0	24.6	3
h	mm	0	991	-

Deleted: ¶
Deleted: Summary
Formatted: Space After: 8 pt
Deleted: net radiation (R_n),
Formatted: Subscript
Formatted: Subscript
Deleted: relative humidity (RH), wind speed (*u*), wind direction (WD)
Formatted: Subscript
Deleted: Note: The negative sign in brackets is due to the sign convention used in the study.
Deleted: 1
Deleted: 2
Deleted: -
Deleted: R_n
Deleted: W m^{-2}
Deleted: -80.5
Deleted: 227.1
Deleted: 39.4
Deleted: T_a
Deleted: °C
Deleted: -19.5
Deleted: 13.1
Deleted: -2.5
Deleted: *u*
Formatted: Font color: Red
Deleted: WD
Deleted: [°]
Deleted: 28
Deleted: 245
Deleted: 148
Deleted: RH
Deleted: %
Deleted: 8
Deleted: 98
Deleted: 43.3
Formatted: Font: Italic
Deleted: *P*
Deleted: mm w.e
Deleted: 0
Deleted: 24.6
Deleted: 3.0
Deleted: h

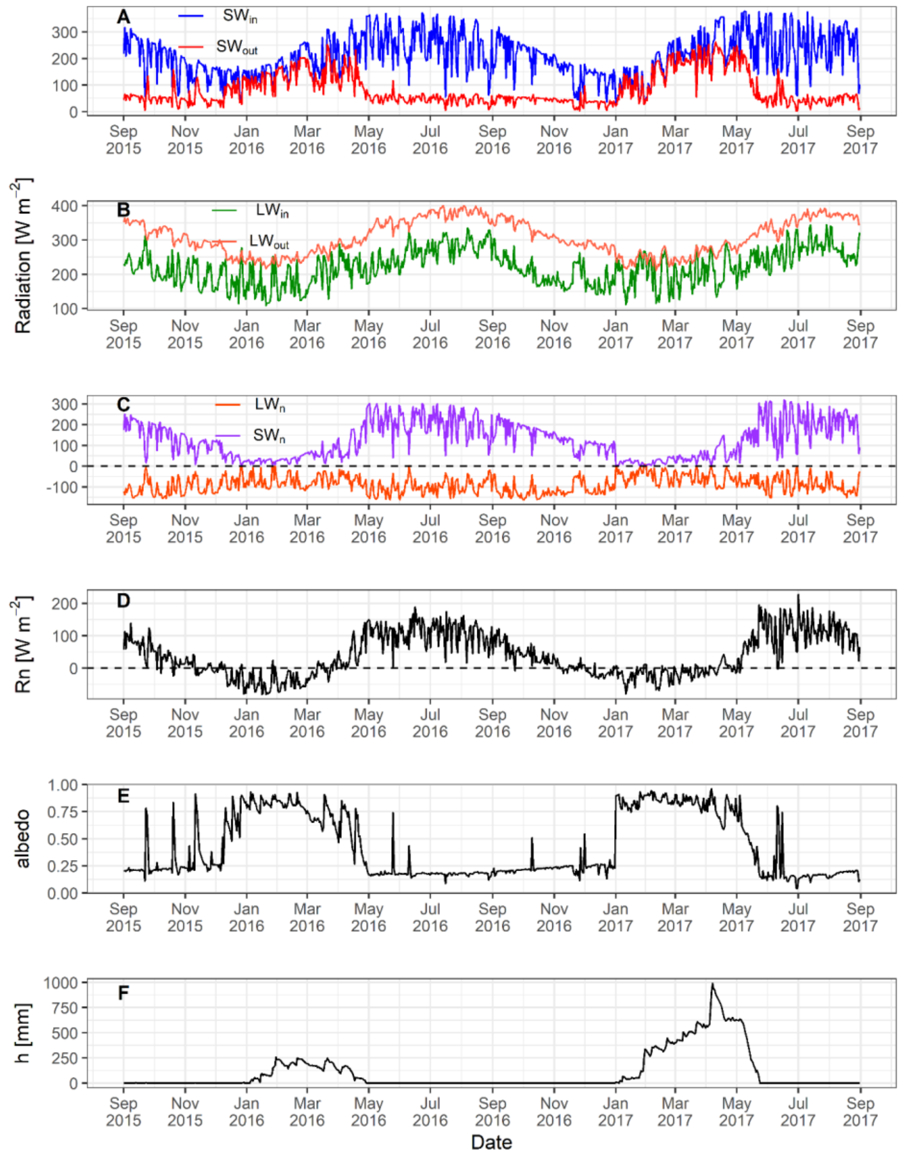

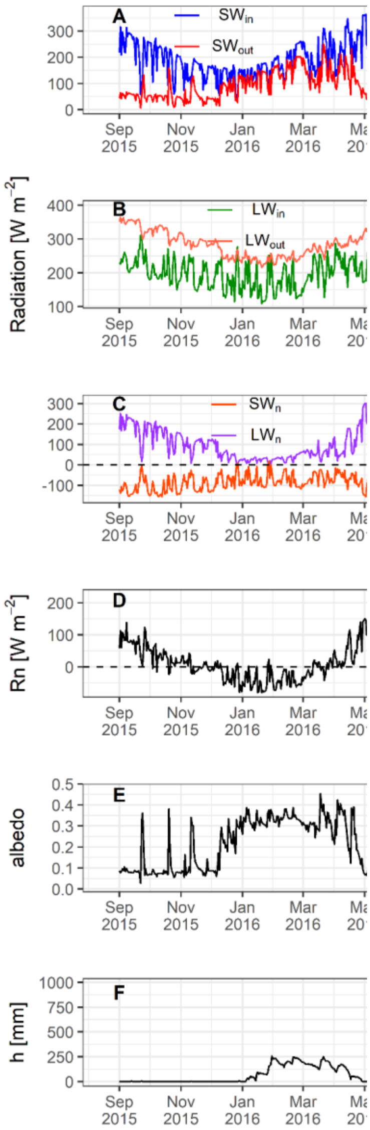

Deleted:

Figure 6 Observed daily mean values of (A) incoming (SW_{in}) and outgoing (SW_{out}) shortwave radiation, (B) incoming (LW_{in}) and outgoing longwave (LW_{out}) radiation, (C) net shortwave (SW_n) and longwave radiation (LW_n), and (D) net radiation (R_n), (E) surface albedo and (F) snow depth (h, mm) at South-Pullu (4727 m a.s.l.) from 1 September 2015 to 31 August 2017.

Deleted: 3 Observed

4.4 Modelled surface energy balance

The mean daily variability of modelled surface energy balance (SEB) components is shown in Figure 7. The average daily simulated R_n ranges between -78.9 to 175.6 W m^{-2} with a mean value of 29.7 W m^{-2}. The R_n shows the seasonal variability and decreases as the ground surface gets covered by seasonal snow cover during wintertime, and increases as the ground surface become snow-free (Figure 7A). From December to March of both the years (2015-16 and 2016-17), R_n decreases and is negative during snow accumulation and remains close to zero during the melting time. For the rest of the time, R_n remains positive. The simulated R_n matches the observed R_n (Figure 7A), which shows that the LW_{out} was estimated very well by the model. The daily mean H ranges between -88.6 to 53 W m^{-2} with a mean value of -15.6 W m^{-2}. The H is positive from January to April (2015-16) and January to June (2016-17) due to the presence of seasonal snow cover (Figure 7B). Rest of the period H remain negative and larger (~35 W m^{-2}) for most of the time. The seasonal variation in H points to a broader temperature gradient in summer than in winter. The daily mean LE ranges between -81.4 to 7.6 W m^{-2} with a mean value of -11.2 W m^{-2}. During the snow-free freezing period (October to December) of both the years, the LE increases (from negative to zero) due to the freezing of moisture content in the soil and also fluctuates close to zero. Furthermore, when the seasonal snow is on the ground, the LE is negative, indicating sublimation and keeps increasing (more negative) after snowmelt indicating evaporation is taking place.

The heat conduction into the ground G remains relatively a smaller component in the SEB (Figure 7C). The mean daily G ranges between -70.9 to 46.3 W m^{-2} with a mean value of -0.5 W m^{-2}. The sign of the G, which shifted from negative during summer to positive during winter, is a function of the annual energy cycle. The heat flux available at the surface for melting (F_{surf}) ranges between -137 to 46.3 W m^{-2} with a mean value of -2.8 W m^{-2} (Table 3). During the summer, when snow melting conditions were prevailing, the F_{surf} turns negative as a result of

Deleted: 4
Deleted: The sign convention adopted is as, energy is considered as gain for the surface or system, if R_n is positive and negative for H and LE. Conversly, energy is considered as loss for the surface or system, if R_n is negative and positive for H and LE (Endrizzi, 2007; Oke, 2002).
Deleted: 35.4
Deleted: 136.9
Deleted: 28.9
Deleted: 4A
Formatted: Subscript
Formatted: Subscript
Formatted: Subscript
Deleted: 34.6
Deleted: 70.4
Deleted: 13.5
Deleted: negative
Deleted: mid-
Deleted: 4B
Deleted: positive
Deleted: 30
Deleted: larger
Deleted: 7.2
Deleted: 71
Deleted: 12
Deleted: 8
Deleted: snow
Deleted: decreases
Deleted: positive
Deleted: positive
Deleted: positive
Deleted:
Formatted: Space After: 8 pt
Deleted: 4C
Deleted: 34.5
Deleted: 67.2
Deleted: 4
Deleted: positive
Deleted: negative
Deleted: 21.8
Deleted: 77.1
Deleted: 1
Deleted: positive

energy available for melt (Figure 7C). The positive F_{surf} during summertime (when melting conditions are prevailing at the surface) is the energy used to refreeze the meltwater and represents the freezing heat flux.

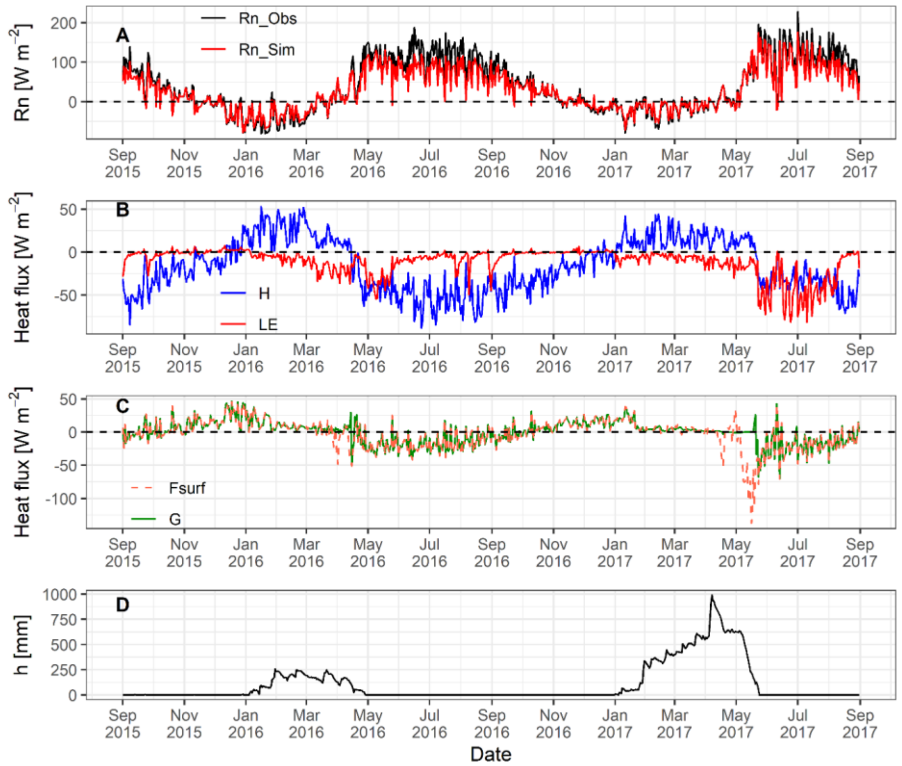

Figure 7 GEOtop simulated daily mean values of surface energy balance components (A) observed and simulated net radiation (R_n), (B) sensible (H) and latent (LE) heat flux, (C) ground heat flux (G) and surface heat flux (F_{surf}) and (D) snow depth (h) at South-Pullu (4727 m a.s.l.) from 1 September 2015 to 31 August 2017.

Deleted: 4C

Deleted: Otherwise, the F_{surf} become zero.

Formatted: Subscript

Deleted:

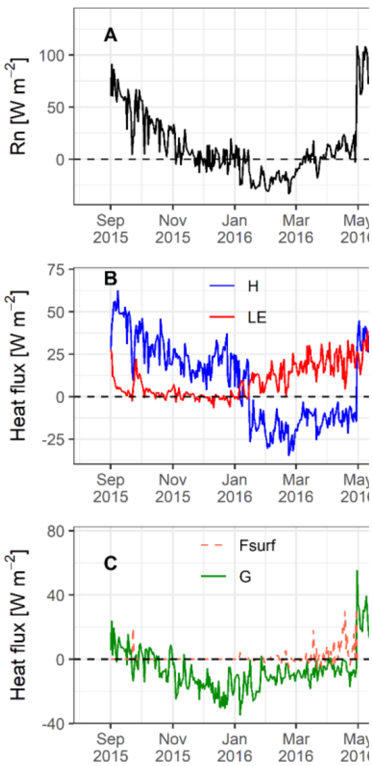

Deleted: 4

Formatted: Subscript

Table 3 Mean daily range of GEOtop simulated SEB (W m^{-2}) components for the study period (1 September 2015 to 31 August 2017) at South-Pullu (4727 m a.s.l.).

Variable	Min.	Max.	Mean
R_n	-78.9	175.6	29.7
H	-88.6	53.0	-15.6
LE	-81.4	7.6	-11.2
G	-70.9	46.3	-0.5
F_{surf}	-137.0	46.3	-2.8

The average season diurnal variation of modelled SEB components (R_n, LE, H and G) for the 2015–16 and 2016–17 years are shown in Supplementary Figures *S6* and *S7*, respectively. The seasons chosen were pre-winter (Sep to Dec), winter (Jan to Apr), post-winter (May-Jun), and summer (Jul to Aug).

In the 2015–16 year (Figure *S6*), the amplitude of R_n and the G during pre-winter, post-winter and summer season were the largest and smallest in winter. The G peaks earlier than those of the LE and H during the pre-winter, post-winter and summer season. The LE and H show strong seasonal characteristics such as (a) during the pre-winter season, the magnitude of diurnal variation of H was greater than LE depicting lesser soil moisture content because of freezing conditions at that time, (b) during the winter season, the amplitude of LE was slightly greater (sublimation process) than H, (c) during the post-winter, the amplitude of H was greater than LE and, (d) during the summer season, again the amplitude of H was greater than LE, which is similar to that of the pattern seen during the pre-winter season. In the 2015-16 year, the amplitude of LE in comparison to H was smaller in summer season due to the lesser precipitation and lesser moisture availability. The R_n and G increased rapidly after the sunrise and changed the direction during pre-winter, post-winter and summer seasons. After sunset, the R_n and G again change sign rapidly, but the LE and H gradually decreased to lower values.

Deleted: 35
Deleted: 4
Deleted: 136.9
Deleted: 28.9
Deleted: -34.6
Deleted: 70.4
Deleted: 13.5
Deleted: -7.2
Deleted: 71.0
Deleted: 12.8
Deleted: -34.5
Deleted: 67.2
Deleted: 0.4
Deleted: -21.8
Deleted: 77.1
Deleted: 2.1
Formatted: Space After: 8 pt
Deleted: *S3*
Deleted: *S4*
Formatted: Font: Not Italic
Deleted: Clear sky days like 14 December 2015 (pre-winter), 18 February 2016 (winter), 30 April 2016 (post-winter), and 31 August 2016 (summer) were selected for the 2015–16 year (Figure *S3*). Similarly, for the 2016–17 year, the following representative days were selected: 14 December 2016, 23 February 2017, 28 April 2017, and 17 August 2017 (Figure *S4*). During the representative days of both the years, the major difference was the changing amplitude of the energy fluxes.
Deleted: *S3*
Deleted: of low snow year
Deleted: LE
Deleted: and H was more or less equal
Deleted: LE
Deleted: (higher soil moisture content and evaporation rate) and comparable to
Deleted: H
Deleted: opposite
Deleted: However, during winter season the G was close to zero.
Deleted: from negative to positive
Deleted: became negative

The LE and H in the morning increased 1 to 2 hours after the R_n during pre-, post-winter and summer season.

In the 2016–17 year (Figure *S7*), the pre-winter, winter and summer were the same as that of the 2015–16 year except for the amplitude of LE in was larger in summer season due to the more precipitation and more moisture availability. However, during the winter and post-winter season of the 2016–17 year, the main difference in diurnal changes was found because of the extended snow cover till May during that year. The amplitude of R_n, LE, H and G were smaller compared to the 2015-16 year.

During the study period, the proportional contribution shows that the net radiation component dominates (80%) the SEB followed by H (9%) and LE fluxes (5%). The G was limited to 5% of the total flux, and 1% was used for melting the seasonal snow. The proportional contribution of each flux percentages of the energy fluxes was calculated by following the approach of Zhang et al. (2013). The mean monthly modelled SEB components for both the years are given in Table *S2*.

Furthermore, during the study period, the partitioning of energy balance shows that 52% (-15.6 W m^{-2}) of R_n (29.7 W m^{-2}) was converted into H, 38% (-11.2 W m^{-2}) into LE, 1% (-0.5 W m^{-2}) into G and 9% (-2.8 W m^{-2}) for melting of seasonal snow. The partitioning was calculated by taking the mean annual average of each of the individual SEB components (LE, H and G) and then divide these respective averages with the mean annual average of R_n. However, a distinct variation of energy flux is observed during the month of May-June, when one of the years (2016-17) experienced extended snow.

4.5 Comparison of seasonal distinction of SEB during low and high snow years

A seasonal distinction of observed radiation (SW_{in}, LW_{in}, SW_{out}, LW_{out}, SW_n, LW_n,) and modelled SEB components (R$_n$, LE, H, G and F_{surf}) for the low and high snow years of the

Deleted: *S4*

Formatted: Space After: 8 pt

Deleted: (28 April 2017)

Deleted: were

Deleted:

Formatted: Subscript

Deleted: was slightly larger. However, all other components (

Deleted:)

Deleted: of almost zero amplitude.

Formatted: Space After: 8 pt

Deleted: Seasonal

Deleted: (SW_n, LW_n,

study period is analysed (Table 4). The seasons were defined as winter (Sep-April) and summer (May-Aug) (Table 4). These seasons were further divided into two sub-seasons each such as early winter (Sep, Oct, Nov and Dec) and peak winter with snow (Jan, Feb, Mar and Apr). Similarly, the summer season was divided into two sub-seasons called early summer (May and June; some years with extended snow) and peak summer (July and August).

Table 4: Mean seasonal values of observed radiation and modelled surface energy balance components.

SEB Components [$W\ m^{-2}$]	2015-16				2016-17			
	Winter (Sep to Apr)		Summer (May to Aug)		Winter (Sep to Apr)		Summer (May to Aug)	
	Sep to Dec (Non-Snow)	Jan to Apr (Snow)	May to Jun (Non-Snow)	Jul-Aug (Peak Summer)	Sep to Dec (Non-Snow)	Jan to Apr (Snow)	May to Jun (Extended Snow)	Jul[illegible] (P[illegible] Sum[illegible]
SW_{in}	177.7	196.0	271.3	245.8	179.2	192.1	262.9	25[illegible]
LW_{in}	203.0	190.5	244.5	286.5	198.0	202.5	245.9	27[illegible]
SW_{out}	57.5	135.4	49.9	44.3	41.0	156.4	86.7	4[illegible]
LW_{out}	310.3	259.5	379.1	412.4	317.9	251.9	337.9	39[illegible]
SW_n	120.2	60.5	221.4	201.5	138.3	35.7	176.2	21[illegible]
LW_n	-107.2	-69.0	-134.5	-125.9	-119.9	-49.4	-92.0	-1[illegible]
R_n	12.9	-8.5	86.9	75.6	18.4	-13.7	84.2	8[illegible]
LE	-1.2	-11.5	-18.9	-7.5	-1.1	-7.7	-33.1	-3[illegible]
H	-21.7	15.7	-47.6	-54.0	-24.3	16.1	-15.9	-4[illegible]
G	10.0	6.8	-20.3	-14.1	7.0	6.2	-14.6	-1[illegible]
F_{surf}	0.1	2.5	0.0	0.1	0.0	0.9	20.6	[illegible]

The mean seasonal variability of energy fluxes during these four major seasons is shown in Table 4. The mean seasonal SW_{in} were comparable for all the seaons whereas SW_{out} was significantly higher (86.7 W m^{-2}) during early summer season of 2016-17 period on account of extended snow cover as compared to the preceeding low snow year (49.9 W m^{-2}). Similarly, LW_{in} show comparable seasonal values during the observation period and LW_{out} show a major difference during the early summer season with extended snow in 2016-17 reducing LW_{out} (337.9 W m^{-2}) as compared to corresponding period in 2015-16 (379.1 W m^{-2}).

Both the years observed comparable SW_n during the early winter period. However, during the peak snow season of the 2016-17 year, the SW_n was comparatively smaller (35.7 W m^{-2}) as

Deleted: but without snow
Deleted: are assessed by considering
Deleted: , early winter (Sep-Dec), peak winter (Jan-April) and early summer (May-June) and peak summer (July-Aug.) of modelled SEB
Deleted: during the designated summer and winter seasons is reported in
Deleted: was highly variable during both the years, and the values of SW_{in}
Deleted: .
Deleted: The
Deleted:
Formatted: Subscript
Deleted: also show
Formatted: Subscript
Formatted: Subscript
Deleted: seasonal variability, but the main difference in ...
Formatted: Subscript
Deleted: sub-season
Deleted: ,
Deleted: when the SW_{out} was 86.7 W m^{-2} (2016-17) in ...
Formatted: Subscript
Formatted: Superscript
Deleted:
Deleted: (2015-16)
Deleted: The
Formatted: Subscript
Deleted: was smaller (190.5 W m^{-2}) in 2015-16 during the ...
Formatted: Superscript
Formatted: Superscript
Deleted: . However, the
Formatted: Subscript
Deleted: sub-season. The mean seasonal LW_{out} was smaller
Formatted: Subscript
Deleted: in the 2016-17 year in comparison
Formatted: Superscript
Deleted:
Formatted: Superscript
Deleted: The SEB results show that the mean seasonal SW ...
Deleted: snow
Deleted: snow-free
Deleted: sub-
Deleted: 50.8
Deleted: during the snow sub-season of the 2016-17

compared to 2015-16 (60.5 W m^{-2}). Similarly, comparable SW_n during the peak summer season of both the years is contrasted by lower SW_n (176.2 W m^{-2}) of early summer period of 2017 as compared to 221.4 W m^{-2} in 2016 on account of extended snow cover. The same trend is recorded for LW_n as well with a lower value during the extended snow (-92 W m^{-2}) in 2017 as compared to 2016 (-134.5 W m^{-2}). Seasonal variations in R_n followed the pattern of SW_n. Both the year's observed comparable R_n during the early snow-free winter period. However, the R_n was comparatively lower (-13.7 W m^{-2}) during the peak snow season of 2016-17 as compared to 2015-16 (-8.5 W m^{-2}). However, most significant difference of R_n is observed during early summer (May-June) and peak summer (Jul-Aug) of 2016 and 2017, respectively. Both the years observed comparable LE flux during the winter season. A key difference in LE flux is observed during extended snow and peak summer sub-season of 2016 and 2017. In the peak summer sub-season of 2016-17, the LE was higher (-31.5 W m^{-2}) as compared to the 2015-16 (-7.5 W m^{-2}). The reason behind this is due to the lesser amount of soil water content availability for evaporation during 2015-16 in comparison to high snow year 2016-17. The comparatively larger LE during the snow sub-season of both the years shows that sublimation is a key factor in the region. The H flux was comparable during the winter season of both the years. During the peak summer sub-season of the 2015-16 year, the H was slightly larger (-54 W m^{-2}) as compared to 2016-17 (-40 W m^{-2}). The critical difference in H flux was observed during the extended snow sub-season of the 2016-17 year when H was much smaller (-15.9 W m^{-2}) compared to 2015-16 (-47.6 W m^{-2}) owing to the extended snow cover during the 2016-17 year.

During the winter season of both the years, the G was positive and changed the sign to negative during the summer season. Overall, G is comparatively a smaller component. The mean seasonal F_{surf} was almost equal to zero during all the seasons except during the snow sub-season of both the years and extended snow sub-season of the 2016-17 year. The F_{surf} (heat flux

Deleted: 5.3

Deleted: ^{2})… Similarly, comparable SW_n was observed during the peak summer sub-…eason of both the years is contrasted by . Key difference is observed during early summer season (May-June) of 2016 and 2017. 2015-16 was a low snow year with early snow melt out and 2016-17 was a high snow year with extended snow cover and late snow melt out. The…ower SW_n (176.2 W m^{-2}) of early summer period period of 2017 as compared to 221.4 W m^{-2} in 2016 on account of extended snow cover.was correspondingly smaller (109.6176.2 W m^{-2}) during the 2017 as compared to 2016.…The LW_n shows less seasonal variability. Both the years observed comparable LW_n during the winter season. However, the …he same trend is recorded for LW_n as well with a was comparatively smaller

Deleted: 61.7

Deleted: and peak summer (-91.6122.3 W m^{-2}) sub-season of

Deleted: the

Deleted: 2016-17…as compared to the May-June

Deleted: 104…34.0

Deleted: and peak summer (-1025.96 W m^{-2}) sub-seasons of 2015-16. The

Deleted: (given by the sum of SW_n and LW_n) …ollowed the pattern of SW_n. Both the year's observed comparable R_n during the early snow

Deleted: smaller

Deleted: 10…3.4

Deleted: sub-

Deleted: the …016-17 as compared to 2015-16 (-4.…9 … W m^{-2}). However, most significant Key

Deleted: The critical

Deleted: The R_n of early summer period was correspondingly larger (80.1 W m^{-2}) during the 2016 as compared to 2017 (47.9). However, an opposite pattern was observed during the peak summer sub-season.

Deleted: The LE flux shows seasonal variability for both the years.

Deleted: and May-June sub-season… Key … key difference in LE flux is observed during extended snow and peak summer sub-season (Jul-Aug) …f 2016 and 2017. In the peak summer sub-season of 2016-17, the LE was higher (-39 31.5 W m^{-2}) as compared to the 2015-16 (11 …7.5 W m^{-2}). The reason behind this is due to the lesser amount of soil water content availability for evaporation during the

Deleted: taking place… key factor in the region. The H flux also shows the seasonal variability.

Deleted: summer …eak summer sub-season of the 2015-16 year, the H was slightly larger (4.1…54 W m^{-2}) as compared to 2016-17 (26.8…40 W m^{-2}). The key …ritical difference in H flux was observed during the extended snow sub-season of the 2016-17 year,…when H was much smaller (-3.4…5.9 W m^{-2}) compared to 2015-16 (36.1

Deleted: . The reason is due

Deleted: negative …ositive and changed the sign to positi

Deleted: The…G was

available for melt) was much higher (20.6 W m^{-2}) during the extended snow sub-season of the 2016-17 year. From the inter-year seasonal comparison, it was found that the extended snow sub-season of the 2016-17 (high snow year) forced significant differences in energy fluxes between the years.

5 Discussion

5.1 A distinction of SEB variations during low and high snow years

Realistic reproduction of seasonal and inter-annual variations in snow depth during the low (2015–16) and high snow (2016–17) years points towards the credible simulation of the SEB during the study period. We further investigated the response of SEB components during these years with contrasting snow cover for a better understanding of the critical periods of meteorological forcing and its characteristics.

To understand the critical periods of meteorological forcing and its effect on modelled SEB fluxes, we will discuss the diurnal variation of modelled SEB only for one season, i.e., early summer season, which showed significant differences in the amplitude of energy fluxes (Figure 8). During the early winter, peak winter and peak summer seasons (Figure *S6*, *S7*), the diurnal variations of the SEB fluxes for the 2015-16 year were more or less similar in comparison to the 2016-17 year. However, during the early summer season of both the years (Figure 8), the SEB fluxes show different diurnal characteristics. During early summer season of the 2016–17 year, the main difference in diurnal changes was found because of the extended snow cover till May during that year. For the 2016–17 year, the amplitude of R_n was slightly larger, whereas, all other components (LE, H and G) were of almost zero amplitude (Figure 8B). The smaller amplitude of LE, H and G is due to the smaller input (solar radiation) and the extended seasonal snow on the ground. Therefore, we can say that the different SEB characteristics during these two years' is in response to the forcing of precipitation via snowfall.

Deleted: a

Deleted: 18

Deleted: showed

Deleted: the

Deleted: major

Deleted: <#>**Model evaluation**¶
<#>In this section, the capability of the 1D GEOtop model to reproduce the point-scale SEB is evaluated. The model was evaluated based on observed radiation components, snow depth and one-year GST. In this study, the simulation results are based on the standard model parameters obtained from the literature (Table 2 and 3, Gubler et al., 2013) and were not improved by trial and error and the same simulation results are used for model evaluation.¶
<#>**Evaluation of radiation components**¶
<#>The first step in our model evaluation was to test the radiation components estimated by the model. The comparison of two-year hourly simulated radiations components SW_{in}, SW_{out}, LW_{in} and LW_{out} against the field observation are shown in Figure 5. The observed and GEOtop estimated SW_{in} shows a strong linear relationship (R^2 = 0.95) and was slightly underestimated (MBD = -5 %) with a high RMSD value of 37 % (Figure 5A). The GEOtop simulated SW_{in} fulfils the criteria of $-5\% \leq$ MBD $\leq 5\%$ set by Badescu et al. (2012) for estimation of global SW_{in} for the Iqbal (1983) model, but the criteria of RMSD $\leq$ 15% is not fulfilled. The SW_{out} also shows good linear relationship (R^2 = 0.84) but it is slightly underestimated (MBD = -1 %) with high RMSD value of 76 % (Figure 5B). The LW_{in} does not show a good linear relationship (R^2 = 0.67) and was slightly overestimated (MBD = 3 %) with RMSD value of 15 % (Figure 5C). The LW_{out} shows a good linear relationship (R^2 = 0.91) but the GEOtop slightly overestimates the LW_{out} (MBD = 2 %) with RMSD value of 8 % (Figure 5D).¶ ...

Deleted: post-winter

Deleted: shows

Deleted: major

Deleted: pre-

Deleted: *S3*

Deleted: *S4*

Deleted: on representative, clear days

Deleted: compared to

Deleted: post-winter

Deleted: the post-winter

Deleted: (28 April 2017)

Deleted: were

Deleted: a reaction

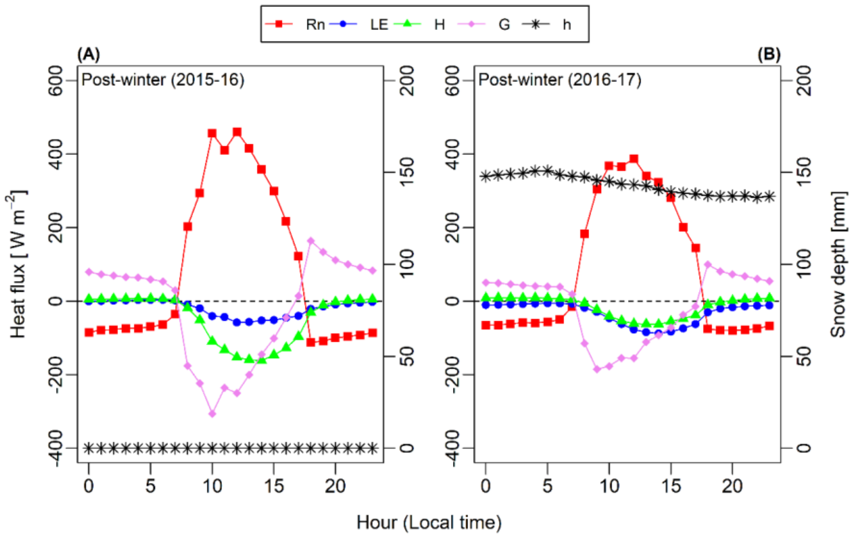

Figure 8 The diurnal change of GEOtop modelled seasonal surface energy fluxes for (A) early summer 2015-16, and (B) early summer 2016-17 at South-Pullu (4727 m a.s.l.), in the upper Ganglass catchment, Leh. The seasonal snow depth is plotted on the secondary axis.

5.2 Impact of freezing and thawing process on surface energy fluxes

To understand the impact of freeze/thaw processes on surface energy fluxes, the variability of SEB components is discussed here (Figure 9). The aim is to make the study site as an exemplar of SEB processes for the seasonal frozen ground and permafrost in the cold-arid Indian Himalayan Region. Comparatively, the R_n was higher at the study site due to the higher elevation, aridity and sparse vegetation.

The freeze and thaw processes in the ground are complex and involve several physical and chemical changes which include energy exchange, phase change, etc. (Chen et al., 2014; Hu et al., 2019). These processes amplify the interaction of fluxes between soil and atmosphere (Chen et al., 2014). In Figure 9D, during the seasonal freezing phase from September to December, the simulated mean monthly G starts to decrease and begins to change the sign from

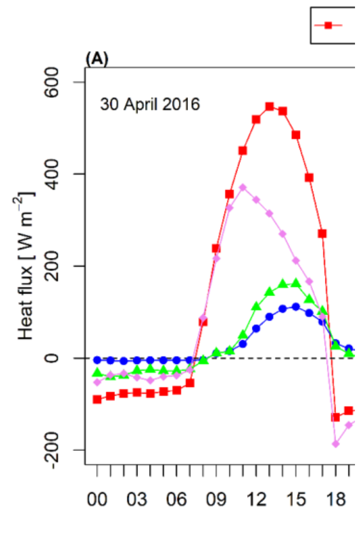

Deleted:

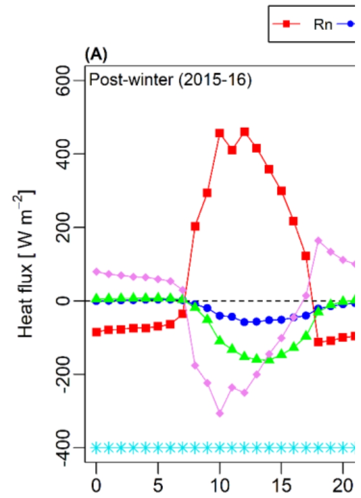

Deleted:

Deleted: on …or (A) 30 April 2016

Deleted: post-winter

Formatted: Space After: 8 pt

Deleted: 28 April 2017

Deleted: post-winter

Deleted: representing post-winter season for the 2015-16 and 2016–17 years respectively

Deleted: ¶

Formatted: Heading 2, Left, Space After: 12 pt, Line spacing: single

Formatted: Subscript

Moved down [6]: In both low and high snow years (Figure 9E, F), the mean monthly H and LE heat fluxes show a

Formatted: Space After: 0 pt

Deleted: ¶

Formatted: Strikethrough

Formatted: Subscript

Formatted: Strikethrough

Field Code Changed

Formatted

negative to positive due to the transfer of flux from soil to the atmosphere. However, during summers, the permafrost and the seasonally frozen soil act as a heat sink, because the thawing processes require a considerable amount of heat that is absorbed from the atmosphere to the soil (Eugster et al., 2000; Gu et al., 2015). In Figure 9D, during the thawing phase from April to July, the simulated mean monthly G starts to increase and changes sign due to the transfer of flux from the atmosphere to the soil. This pattern is consistent with the studies on permafrost areas from the Tibetan Plateau (Chen et al., 2014; Hu et al., 2019; Zhao et al., 2000). In both low and high snow years (Figure 9B and 9C), the mean monthly estimated H and LE heat fluxes show prominent seasonal characteristics, such as the latent heat flux was highest in summer and lowest in winter. In contrast, the sensible heat flux was highest in early summer and gradually decreased towards the pre-winter season. Similar kind of variability in the LE and H is also reported from the seasonally frozen ground and permafrost regions of the Tibetan plateau (Gu et al., 2015; Yao et al., 2011, 2020).

Furthermore, in Figure 9C, during the peak summer months (June to August), the H tends to decrease or became relatively stable. This is mostly due to the thawing in the seasonally frozen ground resulting in a sensible heat sink (Eugster et al., 2000).

In the Tibetan Plateau, the main reasons for the seasonal variability of the turbulent fluxes are due to the Asian monsoon and the freezing and thawing processes of the active layer (Yao et al., 2011), however, in our study site, the monsoon precipitation is not a dominant factor. Therefore, freeze/thaw processes are the key factor regulating the turbulent heat fluxes during summers.

Formatted: Font color: Auto
Field Code Changed
Formatted: Font color: Auto
Formatted: Font color: Auto
Formatted: Font color: Auto
Formatted: Font color: Auto
Formatted: Font color: Auto
Formatted: Font color: Auto
Formatted: Font color: Auto
Deleted: ¶
Deleted: post-winter
Deleted: s
Deleted: does not cross the Himalayan range
Deleted: in this region, during summers, only the
Deleted: going to affect
Deleted: .

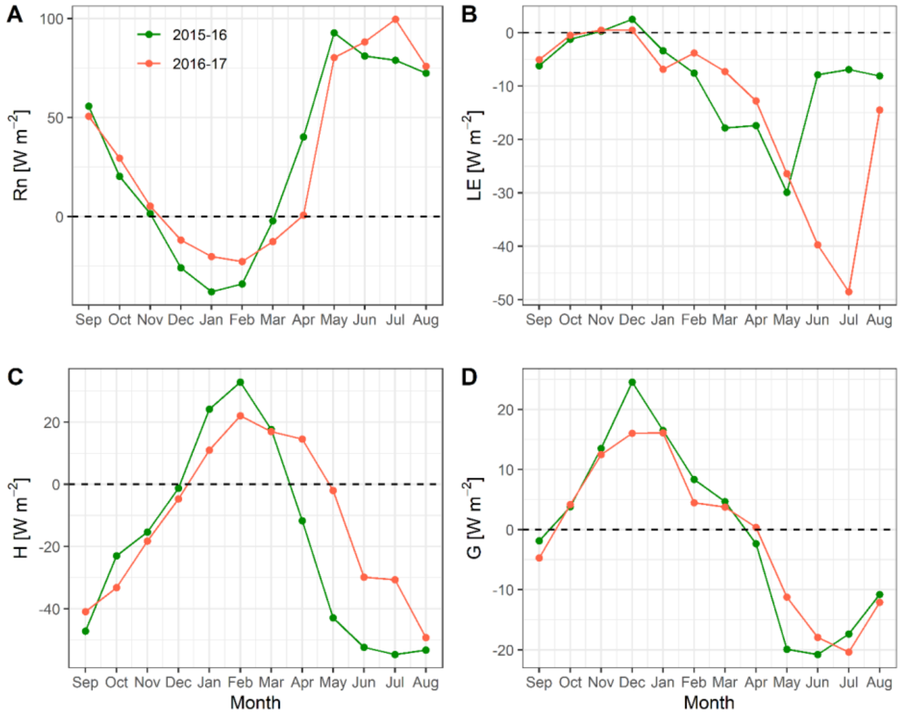

Figure 9: Comparison of estimated mean monthly surface energy balance components (W m^{-2}) (A) R_n, (B) LE, (C) H, and (D) G for the low (2015-16) and high (2016-17) snow years, at South-Pullu (4727 m a.s.l.).

5.3 Comparison with other environments

In this section, the observed radiation and estimated SEB components from our cold-arid catchment in Ladakh, India are compared with other cryospheric systems, globally (Table 5). Although aiming to represent differing permafrost environments, this comparison also includes SEB studies on glaciers for lack of additional data. In most of the studies referred here, the radiation components are measured, and the turbulent (H and LE) and ground (G) heat fluxes are modelled.

Moved (insertion) [6]

Deleted: In both low and high snow years (Figure 9E, F), the mean monthly H and LE heat fluxes show a seasonal characteristic, such as the H was higher than the LE from September to December for both the years. But for the low snow year, the H was lower than the LE from January to April and after that from May to August again the H was higher than LE. In the high snow year, the LE was higher than the H from January to July and was positive pointing towards the sublimation (January to May) and evaporation processes (June to August).¶
In early October, the LE began to weaken up to the December for both the years as the seasonally frozen ground began to freeze. Therefore, the seasonal freezing/thawing of the ground affect the LE causing its rapid decrease/increase. Early in October/November, when the seasonally frozen ground began to freeze, the H did not show any significant variability. However, during summer (from April onwards in 2015–16 and from May onwards in 2016–17), after the snowmelt, the H increases significantly. Similar kind of variability in the LE and H is also reported from the seasonally frozen ground and permafrost regions of the Tibetan plateau (Gu et al., 2015; Yao et al., 2011, 2020).

Formatted: Left, Space After: 8 pt

Deleted: ¶

Deleted: <#>**Influence of snow cover on near-surface ground temperature**¶
<#>The interactions between snow cover and near-surface ground temperature (GST) are complex. Snow cover affects the ground thermal regime by altering the surface energy balance due to its unique characteristics such as, (a) high albedo, (b) high absorptivity, (c) low thermal conductivity, and (d) high latent heat due to snowmelt that is a heat sink (Goodrich, 1982; Gruber, 2005; Zhang, 2005). In comparison to other natural ground surface materials, the low thermal conductivity allows the snow cover to act as an insulator between the atmosphere and the ground. To analyse the effects of snow cover on GST, we plotted the relationship between observed snow depth and GST during the seasonal snow period from 1 January to 23 April 2017 at South-Pullu (4727 m a.s.l.) (Figure 10). For the shallow snow depth, the GST was smaller, and as the depth of snowpack starts increasing, the GST also starts increasing towards 0 °C. The GST varied from -10 °C to about -2 °C under 40 and 900 mm of snow, respectively. During the low snow year, the modelled snow depth show no or small insulating effect on GST (Figure S7). However, during the high snow year, the variations of GST are dampened with increasing snow depth. Furthermore, during the high snow year, only the modelled snow depth greater than 350 mm shows an insulating effect on GST.¶
<#>The timing of snow cover start and its duration has a non-linear influence on the ground surface temperatures (Bartlett et al., 2004). In the early winter, a thin snow cover can cool the ground, whereas a thick snow cover insulates the ground from cold air temperature variations (Keller and Gubler, 1993). During both the years, the snowfall in the catchment occurred by the last week of December facilitating the ground cooling by almost three months (October to December) of sub-zero temperatures up to -20 °C. This could be a key factor in controlling the thermal regime of permafrost in the area. Extended snow cover during the high snow year insulates the ground from ...

Deleted: other

Based on the comparison, the SW_{in} at the study site is comparable with Tibetan plateau (Mölg et al., 2012; Zhang et al., 2013; Zhu et al., 2015) and significantly much higher than the values reported from other studies such as the Alps (Oerlemans and Klok, 2002; Stocker-Mittaz, 2002). The LW_{in} at the study site was comparable with values observed at Tibetan Plateau (Zhang et al., 2013; Zhu et al., 2015) and smaller than the other studies except for Antarctica. At the study site, the SW_n was the largest source of energy and LW_n the most considerable energy loss and strongly negative, and both were higher than those reported in other studies (Table 5). However, the Andes were an exception (Favier, 2004; Pellicciotti et al., 2008).

The different surface albedo (α) values help to distinguish the surface characteristics. The mean α for all the sites (Table 5) where radiation balance is measured either on bedrock or tundra vegetation was smaller than those measured over firn or ice during summer with few exceptions. Albedo ranges for glacier ice from 0.5 to 0.7 and for tundra/bedrock from 0.25 to 0.54. Comparison of RH for the study period shows that the mean measured RH (43 %) was much smaller than other regions except in the semi-arid Andes (Pellicciotti et al., 2008), where the RH was comparable. Furthermore, the mean annual precipitation in this study was also lower than in the other areas compared.

Based on the comparison of measured radiation and meteorological variables with other, better-investigated regions of the world (Table 5), it was observed that our study area is unique in terms of lower RH (43% compared to ~70% in the Alps) and cloudiness, leading to (a) Reduced LW_{in} and strongly negative LW_n (~90 W m^{-2} on average, much more than in the Alps). Hence, the high elevation cold-arid region land surfaces could be overall colder than the locations with more RH. (b) Increased SW_{in}. This will mean that sun-exposed slopes will receive more radiation and shaded ones less (less diffuse radiation) than in comparable areas, and (c) Increased cooling by stronger evaporation in wet places such as meadows. Therefore, the warm sun-exposed dry areas and colder wet places could lead to significant spatial inhomogeneity in

Formatted: Subscript

Formatted: Subscript

Formatted: Font: 11 pt

Deleted: ¶
The mean SW_{in} measured (210 W m^{-2}) in this study site was comparable with values reported from the Tibetan Plateau (200 W m^{-2}) but lower than the Andes (239 W m^{-2}) and significantly higher than the values reported from other studies such as the Alps (136 W m^{-2}).

Deleted: 49

Deleted: 69

Deleted: The mean LW_{in} (220.4 W m^{-2}) observed at Leh station is comparable with values observed at Tibetan Plateau (221 W m^{-2}) and smaller than the other studies except for Antarctica (184.1 W m^{-2}). In the present study, the mean SW_n is the largest source of energy gain (127 W m^{-2}) and LW_n the largest energy loss and strongly negative (-87.6 W m^{-2}) and both were higher than in other studies. However, the SW_n (127 W m^{-2}) observed at Leh station was comparable with the values observed in the tropical Andes (123 W m^{-2}). T

Deleted: , and

Deleted: are both smaller

Deleted: smaller

Deleted: have a very

Deleted: 40

Deleted: (Give value here)

Deleted: This will lead to surfaces being overall colder than at a similar location with more RH,

Deleted: .

permafrost distribution. Further, it is apprehended that high incoming shortwave radiation over moist high elevation surfaces may be facilitating enhanced cooling of as a result of stronger evaporation.

Deleted: in the region

Deleted: wet valley bottom surfaces

Deleted: Where there is enough water, you can cool the ground significantly.¶

Formatted: Font:

Table 5: Comparison of mean annual observed radiation and estimated SEB components and meteorological variables with different regions of the world. (SW_{in} = Incoming shortwave radiation, SW_{out} = Outgoing shortwave radiation, albedo = α, LW_{in} = Incoming longwave radiation, LW_{out} = Outgoing longwave radiation, SW_n = Net shortwave radiation, LW_n = Net longwave radiation, RH = Relative humidity, R_n = Net radiation, LE = Latent heat flux, H = Sensible heat flux, G = Ground heat flux, SEB = energy available at surface, MAAT = Mean annual air temperature, P = Precipitation, NA = Not available). The LE, H, and G are the modelled values. All the radiation components and heat fluxes are in units of W m^{-2}.

Deleted: other

Variable	Leh	Tibetan Plateau	Swiss Alps		Tropical Andes	Semi-arid Andes	New Zealand (Alps)	Canada	Sub-Arctic	Greenland	High Arctic (Norway)				Antarctic	
SW_{in}	210.4	230	136	149	239	344	140	136	101.3	110	79.5	122	78	108	124	94.2
SW_{out}	-83.4	-157	-72	-74	-116	-106	-93	-94	-25.7	-70	-39.5	-38	-42	-70	-79.7	-52.0
α (-)	0.40	0.68	0.53	0.5	0.49	0.3	0.66	0.69	0.25	0.64	0.50	0.31	0.54	0.65	0.64	0.55
LW_{in}	220.4	221	NA	260	272	252	278	248	310	246	263.7	261	254	272	NA	184.1
LW_{out}	-308.0	-277	NA	-308	-311	306	-305	-278	-349.8	-281	-299.0	-300	-286	-292	NA	-233.2
SW_n	127.0	73	64	75	123	238	48	42	75.6	40	40.0	84	36	38	44.3	42.2
LW_n	-87.6	-56	-36	-48	-39	-54	-27	-30	-39.8	-36	-35.3	-39	-32	-20	-49.2	-49.1
RH (%)	43.3	59	64	59	81	42	78	71	~75	75	74.8	83	74	77.9	50.8	69.4
R_n	39.4	17	28	27	84	184	21	12	37.1	4	4.78	45	4	18	-4.9	-6.9

Formatted Table

LE	-11.2	-11	6	-1	-27	-19	1	-15	NA	NA	NA	NA	6.8	1	-62.1	-5.[illegible]
H	-15.6	13	36	-3	21	56	30	-5	2.9	NA	NA	-34.2	-6.9	15	28	12.[illegible]
G	-0.5	2	3	-2	NA	3	2	0.5	1.9	NA	NA	-3.5	~0.5	3	-0.12	0.2
MAAT (°C)	-2.5	-6.3	2.1	-1.1	0.3	NA	1.2	-4.2	6	-5.45	-2.86	-3.4	-5.4	-1.9	-10.2	-18.8
P (mm)	114	1250	NA	NA	970	NA	NA	NA	369	NA	581.2	800	NA	NA	NA	NA
Time period	Sep 2015 to Aug 2017	Aug 2010 to Jul 2012	Jan to Dec 2000	Feb 1997 to Jan 1998	Mar 2002 to Mar 2003	11 Dec 2005–12 Feb 2006	Oct 2010 to Sep 2012	2002-2013	Jan to Dec 2013	Aug 2003 to Aug 2007	Jan 2015 to Dec 2015	Jan to Dec 2000	Mar 2008 to Mar 2009	Sep 2001 to Sep 2006	Mar 2007 to Jan 2013	Apr 1988 to Mar 1989
Surface type	Bedrock/debris	Glacier ice	Glacier ice	Bedrock/debris	Glacier ice	Glacier ice	Glacier ice	Glacier ice	Peatland	Glacier ice	Tundra vegetation	Bedrock/debris	Tundra vegetation	Glacier ice	Ice sheet	Ice sheet
Location	Cold-arid, Ladakh	Zhadang Glacier, Tibetan Plateau	Morteratschgletsche glacier, Switzerland	Murtèl-Corvatsch rock glacier,	Antizana glacier 15, Ecuador	Juncal Norte Glacier, central Chile	Brewster Glacier, New Zealand	Haig Glacier, Canadian rocky mountains	Peatland complex Stordalen, Sweden	west Greenland ice sheet	Bayelva, Spitsbergen, Norway	Juvvasshøe, southern Norway	Svalbard, Norway	Storbreen glacier, Norway	Schirmacher Oasis, Antarctica	Dronning Maud Land, Antarctica
Elevation (m)	4727	5665	2100	2700	4890	3127	1760	2665	380	490	25	1894	25	1570	142	1150

Deleted: 12.8

Deleted: 13.

Deleted: 4

Source	**Latitude**
This Study	34.255° N
(Zhu et al., 2015)	30.476° N
(Oerlemans and Klok, 2002)	46.400° N
(Stocker-Mittaz, 2002)	46.433° N
(Favier, 2004)	0.467° S
(Pellicciotti et al., 2008)	32.99056° S
(Cullen and Conway, 2015)	44.084° S
(Marshall, 2014)	50.717° N
(Stiegler et al., 2016)	68.349° N
(van den Broeke et al., 2008)	67.100° N
(Boike et al., 2018)	78.551° N
(Isaksen et al., 2003)	61.676° N
(Westermann et al., 2009)	78.917° N
(Giesen et al., 2009)	61.600° N
(Ganju and Gusain, 2017)	70.733° S
(Bintanja et al., 1997)	74.481° S

6 Conclusion

In the high-elevation, cold–arid regions of Ladakh significant areas of permafrost occurrence are highly likely (Wani et al., 2020) and large areas experience deep seasonal freeze-thaw. The present study is aimed at providing first insight on the surface energy balance characteristics of this permafrost environment.

For the period under study, the surface energy balance characteristics of the cold-arid site in the Indian Himalayan region show that the net radiation was the major component with a mean value of 29.7 W m^{-2}, followed by sensible heat flux (-15.6 W m^{-2}) and latent heat flux (-11.2 W m^{-2}), and the mean ground heat flux was equal to -0.5 W m^{-2}. During the study period, the partitioning of surface energy balance shows that 52% of R_n was converted into H, 38% into LE, 1% into G and 9% for melting of seasonal snow.

Among the two observation years, one was a low snow year, and the another was high, and during these low and high snow years, the energy utilised for melting seasonal snow was 4% and 14% of R_n, respectively. During both the years, the latent heat flux was highest in summer and lowest in winter, whereas the sensible heat flux was highest in post-winter and gradually decreased towards the pre-winter season. For both low and high years, the snowfall in the catchment occurred by the last week of December facilitating the ground cooling by almost three months (October to December) of sub-zero temperatures up to -20 °C. The extended snow cover during the high snow year also insulates the ground from warmer temperature until May. Therefore, the late occurrence of snow and extended snow cover could be the critical factors in controlling the thermal regime of permafrost in the area.

A comparison of observed radiation and meteorological variables with other regions of the world show that the study site/region at Ladakh have a very low relative humidity (RH) in the range of 43% compared to, e.g. ~70% in the Alps. Therefore, rarefied and dry atmosphere of the cold-arid Himalaya could be impacting the energy regime in multiple ways: (a) this results

Deleted: (Wani et al., 2019)

Deleted:

Deleted: The one-dimensional mode of GEOtop model was used to estimate the surface energy balance at South-Pullu (4727 m a.s.l.) in the upper Ganglass catchment from 1 September 2015 to 31 August 2017 using in-situ meteorological data. The model performance was evaluated using measured radiation components, snow depth variations and one-year near-surface ground temperatures which shows good agreement.

Deleted: daily

Deleted: 28.9

Deleted: 13.5

Deleted: 12.8

Deleted: daily

Deleted: 4

Deleted: show

Deleted: 47

Deleted: (13.5 W m^{-2})

Deleted: (28.9 W m^{-2})

Deleted: 44

Deleted: (12.8 W m^{-2})

Deleted: (0.4 W m^{-2})

Deleted: 7

Deleted: (2.1 W m^{-2})

Deleted:

Deleted: (maximum snow depth of 258 mm and duration of 120 days)

Deleted: (maximum snow depth of 991 mm and duration of 142 days)

Deleted: . D

Deleted: 3

Deleted: 15

Formatted: Subscript

Deleted: Key differences in surface energy balance characteristics were observed during early (May-June) and peak (July-August) summer season of the high snow year. For example, the latent heat flux was higher (39 W m^{-2}) during the peak summer of high snow year compared to the low snow year (11 W m^{-2}). However, the sensible heat flux during the early summer season of the high snow year year was much smaller (-3.4 W m^{-2}) compared to the low snow year (36.1 W m^{-2}). The diurnal variation of surface energy balance components show that the extended snowfall during the high snow year affects surface energy balance characteristics at the study site. The air temperature throughout the study period varies between –23.7 to 18.1 °C with a mean annual averag ...

Deleted: the

Deleted: key

Deleted: .

Deleted: This

in the reduced amount of incoming longwave radiation and strongly negative net longwave radiation, in the range of -90 W m^{-2} compared to -40 W m^{-2} in the Alps and therefore, leading to colder land surfaces as compared to the other mountain environment with higher RH, (b) higher global shortwave radiation leads to more radiation received by sun-exposed slopes than shaded ones in comparable areas and wet places such as meadows, etc. experience increased cooling as a result of stronger evaporation. However, sun-exposed dry areas could be warmer, leading to significant spatial inhomogeneity in permafrost distribution. The current study gives a first-order overview of the surface energy balance from the cold-arid Himalaya in the context of permafrost processes, and we hope this will encourage similar studies at other locations in the region, which would significantly improve the understanding of the climate from the region.

Deleted: .

Deleted: Higher

Deleted:

Deleted: greatly

Acknowledgements

John Mohd Wani acknowledges the Ministry of Human Resource Development (MHRD) Government of India (GOI) fellowship for carrying out his PhD work. Renoj J. Thayyen thanks the National Institute of Hydrology (NIH) Roorkee and SERB (Project No. EMR/2015/000887) for funding the instrumentation in the Ganglass catchment. The first insight into the use of GEOtop permafrost spin up scheme by Joel Fiddes is highly acknowledged. We acknowledge the developers of GEOtop, for keeping the software open-source and free. The source code of the GEOtop model 2.0 (Endrizzi et al., 2014) used is freely available at https://github.com/geotopmodel/geotop/tree/se27xx. The analysis of data was performed using R (R Core Team, 2016; Wickham, 2016, 2017; Wickham and Francois, 2016; Wilke, 2019).

Conflicts of interest

The author(s) declare(s) that there is no conflict of interest.

Author contributions

JMW participated in data collection in the field, carried out the data analysis and processing, run the GEOtop model and prepared the manuscript. RJT conceived the study, arranged field instruments, organised fieldwork for instrumentation and data collection, contributed to the data analysis and manuscript preparation. CSPO assisted in data analysis and manuscript preparation. SG assisted in setting up GEOtop model, analysis of results and manuscript preparation.

References

Ali, S. N., Quamar, M. F., Phartiyal, B. and Sharma, A.: Need for Permafrost Researches in Indian Himalaya, J. Clim. Chang., 4(1), 33–36, doi:10.3233/jcc-180004, 2018.

Allen, S. K., Fiddes, J., Linsbauer, A., Randhawa, S. S., Saklani, B. and Salzmann, N.: Permafrost Studies in Kullu District, Himachal Pradesh, Curr. Sci., 111(3), 550–553, doi:10.18520/cs/v111/i3/550-553, 2016.

Azam, M. F., Wagnon, P., Vincent, C., Ramanathan, A. L., Favier, V., Mandal, A. and Pottakkal, J. G.: Processes governing the mass balance of Chhota Shigri Glacier (western Himalaya, India) assessed by point-scale surface energy balance measurements, Cryosph., 8(6), 2195–2217, doi:10.5194/tc-8-2195-2014, 2014.

Badescu, V., Gueymard, C. A., Cheval, S., Oprea, C., Baciu, M., Dumitrescu, A., Iacobescu, F., Milos, I. and Rada, C.: Computing global and diffuse solar hourly irradiation on clear sky. Review and testing of 54 models, Renew. Sustain. Energy Rev., 16(3), 1636–1656, doi:10.1016/j.rser.2011.12.010, 2012.

Baral, P., Haq, M. A. and Yaragal, S.: Assessment of rock glaciers and permafrost distribution in Uttarakhand, India, Permafr. Periglac. Process., (April 2018), 1–26, doi:10.1002/ppp.2008, 2019.

Bertoldi, G., Notarnicola, C., Leitinger, G., Endrizzi, S., Zebisch, M., Della Chiesa, S. and Tappeiner, U.: Topographical and ecohydrological controls on land surface temperature in an alpine catchment, Ecohydrology, 3(2), 189–204, doi:10.1002/eco.129, 2010.

Bhutiyani, M. R.: Mass-balance studies on Siachen Glacier in the Nubra valley, Karakoram Himalaya, India, J. Glaciol., 45(149), 112–118, doi:10.3189/S0022143000003099, 1999.

Bhutiyani, M. R., Kale, V. S. and Pawar, N. J.: Long-term trends in maximum, minimum and mean annual air temperatures across the Northwestern Himalaya during the twentieth century, Clim. Change, 85(1–2), 159–177, doi:10.1007/s10584-006-9196-1, 2007.

Bintanja, R., Jonsson, S. and Knap, W. H.: The annual cycle of the surface energy balance of

Formatted: Justified

Antarctic blue ice, J. Geophys. Res. Atmos., 102(D2), 1867–1881, doi:10.1029/96JD01801, 1997.

Boeckli, L., Brenning, A., Gruber, S. and Noetzli, J.: A statistical approach to modelling permafrost distribution in the European Alps or similar mountain ranges, Cryosph., 6(1), 125–140, doi:10.5194/tc-6-125-2012, 2012.

Boike, J., Wille, C. and Abnizova, A.: Climatology and summer energy and water balance of polygonal tundra in the Lena River Delta, Siberia, J. Geophys. Res., 113(G3), 1–15, doi:10.1029/2007JG000540, 2008.

Boike, J., Juszak, I., Lange, S., Chadburn, S., Burke, E., Overduin, P. P., Roth, K., Ippisch, O., Bornemann, N., Stern, L., Gouttevin, I., Hauber, E. and Westermann, S.: A 20-year record (1998-2017) of permafrost, active layer and meteorological conditions at a high Arctic permafrost research site (Bayelva, Spitsbergen), Earth Syst. Sci. Data, 10(1), 355–390, doi:10.5194/essd-10-355-2018, 2018.

Bolch, T., Kulkarni, A., Kääb, A., Huggel, C., Paul, F., Cogley, J. G., Frey, H., Kargel, J. S., Fujita, K., Scheel, M. and others: The state and fate of Himalayan glaciers, Science (80-.)., 336(6079), 310–314, doi:10.1126/science.1215828, 2012.

Bolch, T., Shea, J. M., Liu, S., Azam, F. M., Gao, Y., Gruber, S., Immerzeel, W. W., Kulkarni, A., Li, H., Tahir, A. A., Zhang, G. and Zhang, Y.: Status and Change of the Cryosphere in the Extended Hindu Kush Himalaya Region, in The Hindu Kush Himalaya Assessment, edited by P. Wester, A. Mishra, A. Mukherji, and A. B. Shrestha, pp. 209–255, Springer, Cham., 2019.

Bommer, C., Phillips, M. and Arenson, L. U.: Practical recommendations for planning, constructing and maintaining infrastructure in mountain permafrost, Permafr. Periglac. Process., 21(1), 97–104, doi:10.1002/ppp.679, 2010.

van den Broeke, M., van As, D., Reijmer, C. and van de Wal, R.: Assessing and Improving the Quality of Unattended Radiation Observations in Antarctica, J. Atmos. Ocean. Technol., 21(9), 1417–1431, doi:10.1175/1520-0426(2004)021<1417:AAITQO>2.0.CO;2, 2004.

van den Broeke, M., Smeets, P., Ettema, J. and Munneke, P. K.: Surface radiation balance in the ablation zone of the west Greenland ice sheet, J. Geophys. Res., 113(D13), 1–14, doi:10.1029/2007JD009283, 2008.

Brutsaert, W.: A theory for local evaporation (or heat transfer) from rough and smooth surfaces at ground level, Water Resour. Res., 11(4), 543–550, doi:10.1029/WR011i004p00543, 1975.

Cao, B., Quan, X., Brown, N., Stewart-Jones, E. and Gruber, S.: GlobSim (v1.0): Deriving meteorological time series for point locations from multiple global reanalyses, Geosci. Model Dev. Discuss., (July), 1–29, doi:10.5194/gmd-2019-157, 2019.

Carslaw, D. C. and Ropkins, K.: openair — An R package for air quality data analysis, Environ. Model. Softw., 27–28, 52–61, doi:10.1016/j.envsoft.2011.09.008, 2012.

Chen, B., Luo, S., Lü, S., Yu, Z. and Ma, D.: Effects of the soil freeze-thaw process on the regional climate of the Qinghai-Tibet Plateau, Clim. Res., 59(3), 243–257, doi:10.3354/cr01217, 2014.

Chiesa, D. D., Bertoldi, G., Niedrist, G., Obojes, N., Endrizzi, S., Albertson, J. D., Wohlfahrt, G., Hörtnagl, L. and Tappeiner, U.: Modelling changes in grassland hydrological cycling along an elevational gradient in the Alps, Ecohydrology, 7(6), 1453–1473, doi:10.1002/eco.1471, 2014.

Cosenza, P., Guérin, R. and Tabbagh, A.: Relationship between thermal conductivity and water content of soils using numerical modelling, Eur. J. Soil Sci., 54(3), 581–588, doi:10.1046/j.1365-2389.2003.00539.x, 2003.

Cullen, N. J. and Conway, J. P.: A 22 month record of surface meteorology and energy balance from the ablation zone of Brewster Glacier, New Zealand, J. Glaciol., 61(229), 931–946, doi:10.3189/2015JoG15J004, 2015.

Dall’Amico, M., Endrizzi, S., Gruber, S. and Rigon, R.: A robust and energy-conserving model of freezing variably-saturated soil, Cryosph., 5(2), 469–484, doi:10.5194/tc-5-469-2011, 2011a.

Dall'Amico, M., Endrizzi, S. and Rigon, R.: Snow mapping of an alpine catchment through the hydrological model GEOtop, in Proceedings Conference Eaux en montagne, Lyon, pp. 16–17., 2011b.

Dall'Amico, M., Endrizzi, S. and Tasin, S.: MYSNOWMAPS: OPERATIVE HIGH-RESOLUTION REAL-TIME SNOW MAPPING, in Proceedings, International Snow Science Workshop, pp. 328–332, Innsbruck, Austria., 2018.

Endrizzi, S.: Snow cover modelling at a local and distributed scale over complex terrain, University of Trento., 2007.

Endrizzi, S., Gruber, S., Dall'Amico, M. and Rigon, R.: GEOtop 2.0: simulating the combined energy and water balance at and below the land surface accounting for soil freezing, snow cover and terrain effects, Geosci. Model Dev., 7(6), 2831–2857, doi:10.5194/gmd-7-2831-2014, 2014.

Engel, M., Notarnicola, C., Endrizzi, S. and Bertoldi, G.: Snow model sensitivity analysis to understand spatial and temporal snow dynamics in a high-elevation catchment, Hydrol. Process., 31(23), 4151–4168, doi:10.1002/hyp.11314, 2017.

Eugster, W., Rouse, W. R., Pielke Sr, R. A., Mcfadden, J. P., Baldocchi, D. D., Kittel, T. G. F., Chapin, F. S., Liston, G. E., Vidale, P. L., Vaganov, E. and Chambers, S.: Land-atmosphere energy exchange in Arctic tundra and boreal forest: available data and feedbacks to climate, Glob. Chang. Biol., 6(S1), 84–115, doi:10.1046/j.1365-2486.2000.06015.x, 2000.

Favier, V.: One-year measurements of surface heat budget on the ablation zone of Antizana Glacier 15, Ecuadorian Andes, J. Geophys. Res., 109(D18), 1–15, doi:10.1029/2003JD004359, 2004.

Fiddes, J. and Gruber, S.: TopoSUB: a tool for efficient large area numerical modelling in complex topography at sub-grid scales, Geosci. Model Dev., 5(5), 1245–1257, doi:10.5194/gmd-5-1245-2012, 2012.

Fiddes, J., Endrizzi, S. and Gruber, S.: Large-area land surface simulations in heterogeneous terrain driven by global data sets: application to mountain permafrost, Cryosph., 9(1), 411–426, doi:10.5194/tc-9-411-2015, 2015.

Ganju, A. and Gusain, H. S.: Six Years Observations ond Analysis of Radiation Parameters and Surface Energy Fluxes on Ice Sheet Near ‘Maitri’Research Station, East Antarctica, Proc. Indian Natl. Sci. Acad., 83(2), 449–460, 2017.

Gao, T., Zhang, T., Guo, H., Hu, Y., Shang, J. and Zhang, Y.: Impacts of the active layer on runoff in an upland permafrost basin, northern Tibetan Plateau, edited by J. A. Añel, PLoS One, 13(2), 1–15, doi:10.1371/journal.pone.0192591, 2018.

Garratt, J. R.: The atmospheric boundary layer. Cambridge atmospheric and space science series, Cambridge University Press., 1994.

Giesen, R. H., Andreassen, L. M., van den Broeke, M. R. and Oerlemans, J.: Comparison of the meteorology and surface energy balance at Storbreen and Midtdalsbreen, two glaciers in southern Norway, Cryosph., 3(1), 57–74, doi:10.5194/tc-3-57-2009, 2009.

Gruber, S. and Haeberli, W.: Permafrost in steep bedrock slopes and its temperature-related destabilization following climate change, J. Geophys. Res., 112(F2), 1–10, doi:10.1029/2006JF000547, 2007.

Gruber, S., Hoelzle, M. and Haeberli, W.: Permafrost thaw and destabilization of Alpine rock walls in the hot summer of 2003, Geophys. Res. Lett., 31(L13504), 1–4, doi:10.1029/2004GL020051, 2004.

Gruber, S., Fleiner, R., Guegan, E., Panday, P., Schmid, M. O., Stumm, D., Wester, P., Zhang, Y. and Zhao, L.: Review article: Inferring permafrost and permafrost thaw in the mountains of the Hindu Kush Himalaya region, Cryosph., 11(1), 81–99, doi:10.5194/tc-11-81-2017, 2017.

Gu, L., Yao, J., Hu, Z. and Zhao, L.: Comparison of the surface energy budget between regions of seasonally frozen ground and permafrost on the Tibetan Plateau, Atmos. Res., 153, 553–564, doi:10.1016/j.atmosres.2014.10.012, 2015.

Gubler, S.: Measurement Variability and Model Uncertainty in Mountain Permafrost Research, University of Zurich., 2013.

Gubler, S., Gruber, S. and Purves, R. S.: Uncertainties of parameterized surface downward clear-sky shortwave and all-sky longwave radiation., Atmos. Chem. Phys., 12(11), 5077–5098, doi:10.5194/acp-12-5077-2012, 2012.

Gubler, S., Endrizzi, S., Gruber, S. and Purves, R. S.: Sensitivities and uncertainties of modeled ground temperatures in mountain environments, Geosci. Model Dev., 6(4), 1319–1336, doi:10.5194/gmd-6-1319-2013, 2013.

Gueymard, C. A.: Clear-sky irradiance predictions for solar resource mapping and large-scale applications: Improved validation methodology and detailed performance analysis of 18 broadband radiative models, Sol. Energy, 86(8), 2145–2169, doi:10.1016/j.solener.2011.11.011, 2012.

Gupta, H. V., Bastidas, L. A., Sorooshian, S., Shuttleworth, W. J. and Yang, Z. L.: Parameter estimation of a land surface scheme using multicriteria methods, J. Geophys. Res. Atmos., 104(D16), 19491–19503, doi:10.1029/1999JD900154, 1999.

Haeberli, W., Noetzli, J., Arenson, L., Delaloye, R., Gärtner-Roer, I., Gruber, S., Isaksen, K., Kneisel, C., Krautblatter, M. and Phillips, M.: Mountain permafrost: development and challenges of a young research field, J. Glaciol., 56(200), 1043–1058, doi:10.3189/002214311796406121, 2010.

Harris, C., Davies, M. C. R. and Etzelmüller, B.: The assessment of potential geotechnical hazards associated with mountain permafrost in a warming global climate, Permafr. Periglac. Process., 12(1), 145–156, doi:10.1002/ppp.376, 2001.

Hasler, A., Geertsema, M., Foord, V., Gruber, S. and Noetzli, J.: The influence of surface characteristics, topography and continentality on mountain permafrost in British Columbia, Cryosph., 9(3), 1025–1038, doi:10.5194/tc-9-1025-2015, 2015.

Hingerl, L., Kunstmann, H., Wagner, S., Mauder, M., Bliefernicht, J. and Rigon, R.: Spatio-temporal variability of water and energy fluxes - a case study for a mesoscale catchment in pre-alpine environment, Hydrol. Process., 30(21), 3804–3823, doi:10.1002/hyp.10893, 2016.

Hock, R., Rasul, G., Adler, C., Cáceres, B., Gruber, S., Hirabayashi, Y., Jackson, M., Kääb, A., Kang, S., Kutuzov, S., Milner, A., Molau, U., Morin, S., Orlove, B. and Steltzer, H.: High Mountain Areas. In: IPCC Special Report on the Ocean and Cryosphere in a Changing Climate [H.-O. Pörtner, D.C. Roberts, V. Masson-Delmotte, P. Zhai, M. Tignor, E. Poloczanska, K. Mintenbeck, A. Alegría, M. Nicolai, A. Okem, J. Petzold, B. Rama, N.M., 2019.

Hu, G., Zhao, L., Li, R., Wu, X., Wu, T., Zhu, X., Pang, Q., Liu, G. yue, Du, E., Zou, D., Hao, J. and Li, W.: Simulation of land surface heat fluxes in permafrost regions on the Qinghai-Tibetan Plateau using CMIP5 models, Atmos. Res., 220, 155–168, doi:10.1016/j.atmosres.2019.01.006, 2019.

Immerzeel, W. W., van Beek, L. P. H. and Bierkens, M. F. P.: Climate Change Will Affect the Asian Water Towers, Science (80-.)., 328(5984), 1382–1385, doi:10.1126/science.1183188, 2010.

Immerzeel, W. W., van Beek, L. P. H., Konz, M., Shrestha, A. B. and Bierkens, M. F. P.: Hydrological response to climate change in a glacierized catchment in the Himalayas, Clim. Change, 110(3–4), 721–736, doi:10.1007/s10584-011-0143-4, 2012.

Immerzeel, W. W., Wanders, N., Lutz, A. F., Shea, J. M. and Bierkens, M. F. P.: Reconciling high-altitude precipitation in the upper Indus basin with glacier mass balances and runoff, Hydrol. Earth Syst. Sci., 19(11), 4673–4687, doi:10.5194/hess-19-4673-2015, 2015.

Isaksen, K., Heggem, E. S. F., Bakkehøi, S., Ødegård, R. S., Eiken, T., Etzelmüller, B. and

Sollid, J. L.: Mountain permafrost and energy balance on Juvvasshøe, southern Norway, in Eight International Conference on Permafrost, vol. 1, edited by M. Phillips, S. Springman, and L. Arenson, pp. 467–472, Swets & Zeitlinger, Lisse, Zurich, Switzerland., 2003.

Jordan, R. E., Andreas, E. L. and Makshtas, A. P.: Heat budget of snow-covered sea ice at North Pole 4, J. Geophys. Res. Ocean., 104(C4), 7785–7806, doi:10.1029/1999JC900011, 1999.

Kaser, G., Grosshauser, M. and Marzeion, B.: Contribution potential of glaciers to water availability in different climate regimes, Proc. Natl. Acad. Sci., 107(47), 20223–20227, doi:10.1073/pnas.1008162107, 2010.

Kodama, Y., Sato, N., Yabuki, H., Ishii, Y., Nomura, M. and Ohata, T.: Wind direction dependency of water and energy fluxes and synoptic conditions over a tundra near Tiksi, Siberia, Hydrol. Process., 21(15), 2028–2037, doi:10.1002/hyp.6712, 2007.

Langer, M., Westermann, S., Muster, S., Piel, K. and Boike, J.: The surface energy balance of a polygonal tundra site in northern Siberia - Part 2: Winter, Cryosphere, 5(2), 509–524, doi:10.5194/tc-5-509-2011, 2011a.

Langer, M., Westermann, S., Muster, S., Piel, K. and Boike, J.: The surface energy balance of a polygonal tundra site in northern Siberia – Part 1: Spring to fall, Cryosph., 5(1), 151–171, doi:10.5194/tc-5-151-2011, 2011b.

Lloyd, C. R., Harding, R. J., Friborg, T. and Aurela, M.: Surface fluxes of heat and water vapour from sites in the European Arctic, Theor. Appl. Climatol., 70(1–4), 19–33, doi:10.1007/s007040170003, 2001.

Lone, S. A., Jeelani, G., Deshpande, R. D. and Mukherjee, A.: Stable isotope (δ18O and δD) dynamics of precipitation in a high altitude Himalayan cold desert and its surroundings in Indus river basin, Ladakh, Atmos. Res., 221(October 2018), 46–57, doi:10.1016/j.atmosres.2019.01.025, 2019.

Lunardini, V. J.: Heat transfer in cold climates, Van Nostrand Reinhold Company., 1981.

Lutz, A. F., Immerzeel, W. W., Shrestha, A. B. and Bierkens, M. F. P.: Consistent increase in High Asia’s runoff due to increasing glacier melt and precipitation, Nat. Clim. Chang., 4(7), 587–592, doi:10.1038/nclimate2237, 2014.

Lynch, A. H., Chapin, F. S., Hinzman, L. D., Wu, W., Lilly, E., Vourlitis, G. and Kim, E.: Surface Energy Balance on the Arctic Tundra: Measurements and Models, J. Clim., 12(8), 2585–2606, doi:10.1175/1520-0442(1999)012<2585:SEBOTA>2.0.CO;2, 1999.

MacDonell, S., Kinnard, C., Mölg, T., Nicholson, L. and Abermann, J.: Meteorological drivers of ablation processes on a cold glacier in the semi-arid Andes of Chile, Cryosph., 7(5), 1513–1526, doi:10.5194/tc-7-1513-2013, 2013.

Mair, E., Leitinger, G., Della Chiesa, S., Niedrist, G., Tappeiner, U. and Bertoldi, G.: A simple method to combine snow height and meteorological observations to estimate winter precipitation at sub-daily resolution, Hydrol. Sci. J., 61(11), 2050–2060, doi:10.1080/02626667.2015.1081203, 2016.

Marshall, S. J.: Meltwater run-off from Haig Glacier, Canadian Rocky Mountains, 2002–2013, Hydrol. Earth Syst. Sci., 18(12), 5181–5200, doi:10.5194/hess-18-5181-2014, 2014.

Martin, E. and Lejeune, Y.: Turbulent fluxes above the snow surface, Ann. Glaciol., 26(1), 179–183, doi:10.3189/1998AoG26-1-179-183, 1998.

Mauder, M., Genzel, S., Fu, J., Kiese, R., Soltani, M., Steinbrecher, R., Zeeman, M., Banerjee, T., De Roo, F. and Kunstmann, H.: Evaluation of energy balance closure adjustment methods by independent evapotranspiration estimates from lysimeters and hydrological simulations, Hydrol. Process., 32(1), 39–50, doi:10.1002/hyp.11397, 2018.

McBean, G. A. and Miyake, M.: Turbulent transfer mechanisms in the atmospheric surface layer, Q. J. R. Meteorol. Soc., 98(416), 383–398, doi:10.1002/qj.49709841610, 1972.

Mittaz, C., Hoelzle, M. and Haeberli, W.: First results and interpretation of energy-flux measurements over Alpine permafrost, Ann. Glaciol., 31, 275–280, doi:10.3189/172756400781820363, 2000.

Mölg, T.: Ablation and associated energy balance of a horizontal glacier surface on Kilimanjaro, J. Geophys. Res., 109(D16), D16104, doi:10.1029/2003JD004338, 2004.

Mölg, T., Maussion, F., Yang, W. and Scherer, D.: The footprint of Asian monsoon dynamics in the mass and energy balance of a Tibetan glacier, Cryosph., 6(6), 1445–1461, doi:10.5194/tc-6-1445-2012, 2012.

Monin, A. S. and Obukhov, A. M.: Basic laws of turbulent mixing in the atmosphere near the ground, Tr. Akad. Nauk SSSR Geofiz. Inst, 24(151), 163–187, 1954.

Mu, C., Li, L., Wu, X., Zhang, F., Jia, L., Zhao, Q. and Zhang, T.: Greenhouse gas released from the deep permafrost in the northern Qinghai-Tibetan Plateau, Sci. Rep., 8(1), 1–9, doi:10.1038/s41598-018-22530-3, 2018.

Nash, J. E. and Sutcliffe, J. V.: River flow forecasting through conceptual models part I — A discussion of principles, J. Hydrol., 10(3), 282–290, doi:10.1016/0022-1694(70)90255-6, 1970.

Nicholson, L. I., Prinz, R., Mölg, T. and Kaser, G.: Micrometeorological conditions and surface mass and energy fluxes on Lewis Glacier, Mt Kenya, in relation to other tropical glaciers, Cryosph., 7(4), 1205–1225, doi:10.5194/tc-7-1205-2013, 2013.

Oerlemans, J. and Klok, E. J.: Energy Balance of a Glacier Surface: Analysis of Automatic Weather Station Data from the Morteratschgletscher, Switzerland, Arctic, Antarct. Alp. Res., 34(4), 477–485, doi:10.1080/15230430.2002.12003519, 2002.

Ohmura, A.: Climate and energy balance on the arctic tundra, J. Climatol., 2(1), 65–84, doi:10.1002/joc.3370020106, 1982.

Ohmura, A.: Comparative energy balance study for arctic tundra, sea surface glaciers and boreal forests, GeoJournal, 8(3), 221–228, doi:10.1007/BF00446471, 1984.

Oke, T. R.: Boundary Layer Climates, Routledge., 2002.

Pandey, P.: Inventory of rock glaciers in Himachal Himalaya, India using high-resolution Google Earth imagery, Geomorphology, 340, 103–115, doi:10.1016/j.geomorph.2019.05.001, 2019.

Pellicciotti, F., Helbing, J., Rivera, A., Favier, V., Corripio, J., Araos, J., Sicart, J.-E. and Carenzo, M.: A study of the energy balance and melt regime on Juncal Norte Glacier, semi-arid Andes of central Chile, using melt models of different complexity, Hydrol. Process., 22(19), 3980–3997, doi:10.1002/hyp.7085, 2008.

PERMOS: Permafrost in Switzerland 2014/2015 to 2017/2018. Noetzli, J., Pellet, C. and Staub, B. (eds.), Glaciological Report Permafrost No. 16-19 of the Cryospheric Commission of the Swiss Academy of Sciences, 104 pp., 2019.

Pogliotti, P.: Influence of snow cover on MAGST over complex morphologies in mountain permafrost regions, University of Torino, Torino., 2011.

Pritchard, H. D.: Asia's shrinking glaciers protect large populations from drought stress, Nature, 569(7758), 649–654, doi:10.1038/s41586-019-1240-1, 2019.

R Core Team: R: A Language and Environment for Statistical Computing, [online] Available from: https://www.r-project.org/, 2016.

Rasmussen, R., Baker, B., Kochendorfer, J., Meyers, T., Landolt, S., Fischer, A. P., Black, J., Thériault, J. M., Kucera, P., Gochis, D., Smith, C., Nitu, R., Hall, M., Ikeda, K. and Gutmann, E.: How Well Are We Measuring Snow: The NOAA/FAA/NCAR Winter Precipitation Test Bed, Bull. Am. Meteorol. Soc., 93(6), 811–829, doi:10.1175/BAMS-D-11-00052.1, 2012.

Rastogi, S. P. and Narayan, S.: Permafrost areas in Tso Kar Basin, in Symposium for Snow, Ice and Glaciers, March 1999, pp. 315–319, Geological Survey of India Special Publication 53., 1999.

Rigon, R., Bertoldi, G. and Over, T. M.: GEOtop: A Distributed Hydrological Model with Coupled Water and Energy Budgets, J. Hydrometeorol., 7(3), 371–388, doi:10.1175/JHM497.1, 2006.

Roberts, K. E., Lamoureux, S. F., Kyser, T. K., Muir, D. C. G., Lafrenière, M. J., Iqaluk, D., Pieńkowski, A. J. and Normandeau, A.: Climate and permafrost effects on the chemistry and ecosystems of High Arctic Lakes, Sci. Rep., 7(1), 1–8, doi:10.1038/s41598-017-13658-9, 2017.

Roesch, A., Wild, M., Pinker, R. and Ohmura, A.: Comparison of spectral surface albedos and their impact on the general circulation model simulated surface climate, J. Geophys. Res., 107(D14), 4221, doi:10.1029/2001JD000809, 2002.

Salzmann, N., Nötzli, J., Hauck, C., Gruber, S., Hoelzle, M. and Haeberli, W.: Ground surface temperature scenarios in complex high-mountain topography based on regional climate model results, J. Geophys. Res., 112(F2), 1–10, doi:10.1029/2006JF000527, 2007.

Schmid, M.-O., Baral, P., Gruber, S., Shahi, S., Shrestha, T., Stumm, D. and Wester, P.: Assessment of permafrost distribution maps in the Hindu Kush Himalayan region using rock glaciers mapped in Google Earth, Cryosph., 9(6), 2089–2099, doi:10.5194/tc-9-2089-2015, 2015.

Sellers, W. D.: Physical climatology, The University of Chicago Press., 1965.

Singh, N., Singhal, M., Chhikara, S., Karakoti, I., Chauhan, P. and Dobhal, D. P.: Radiation and energy balance dynamics over a rapidly receding glacier in the central Himalaya, Int. J. Climatol., 40(1), 400–420, doi:10.1002/joc.6218, 2020.

Soltani, M., Laux, P., Mauder, M. and Kunstmann, H.: Inverse distributed modelling of streamflow and turbulent fluxes: A sensitivity and uncertainty analysis coupled with automatic optimization, J. Hydrol., 571, 856–872, doi:10.1016/j.jhydrol.2019.02.033, 2019.

Stiegler, C., Johansson, M., Christensen, T. R., Mastepanov, M. and Lindroth, A.: Tundra permafrost thaw causes significant shifts in energy partitioning, Tellus B Chem. Phys. Meteorol., 68(1), 1–11, doi:10.3402/tellusb.v68.30467, 2016.

Stocker-Mittaz, C.: Permafrost Distribution Modeling Based on Energy Balance Data, University of Zurich, Switzerland., 2002.

Strugnell, N. C. and Lucht, W.: An Algorithm to Infer Continental-Scale Albedo from AVHRR Data, Land Cover Class, and Field Observations of Typical BRDFs, J. Clim., 14(7), 1360–1376, doi:10.1175/1520-0442(2001)014<1360:AATICS>2.0.CO;2, 2001.

Stull, R. B.: An Introduction to Boundary Layer Meteorology, Springer Netherlands, Dordrecht., 1988.

Thakur, V. C.: Regional framework and geodynamic evolution of the Indus-Tsangpo suture zone in the Ladakh Himalayas, Trans. R. Soc. Edinb. Earth Sci., 72(2), 89–97, doi:10.1017/S0263593300009925, 1981.

Thayyen, R. J.: Ground ice melt in the catchment runoff in the Himalayan cold-arid system, in IGS Symposium on Glaciology in High-Mountain Asia, Kathmandu, Nepal, 1-6 March 2015, Kathmandu, Nepal., 2015.

Thayyen, R. J.: Hydrology of the Cold-Arid Himalaya, in Himalayan Weather and Climate and their Impact on the Environment, pp. 399–417, Springer International Publishing, Cham., 2020.

Thayyen, R. J. and Dimri, A. P.: Factors controlling Slope Environmental Lapse Rate (SELR) of temperature in the monsoon and cold-arid glacio-hydrological regimes of the Himalaya, Cryosph. Discuss., 8(6), 5645–5686, doi:10.5194/tcd-8-5645-2014, 2014.

Thayyen, R. J. and Gergan, J. T.: Role of glaciers in watershed hydrology: a preliminary study of a "Himalayan catchment," Cryosph., 4(1), 115–128, doi:10.5194/tc-4-115-2010, 2010.

Thayyen, R. J., Dimri, A. P., Kumar, P. and Agnihotri, G.: Study of cloudburst and flash floods around Leh, India, during August 4–6, 2010, Nat. Hazards, 65(3), 2175–2204, doi:10.1007/s11069-012-0464-2, 2013.

Thayyen, R. J., Rai, S. P. and Goel, M. K.: Glaciological studies of Phuche glacier, Ladakh Range., 2015.

Wang, G., Li, Y., Wu, Q. and Wang, Y.: Impacts of permafrost changes on alpine ecosystem in Qinghai-Tibet Plateau, Sci. China Ser. D Earth Sci., 49(11), 1156–1169, doi:10.1007/s11430-006-1156-0, 2006.

Wang, X., Chen, R. and Yang, Y.: Effects of Permafrost Degradation on the Hydrological Regime in the Source Regions of the Yangtze and Yellow Rivers, China, Water, 9(11), 1–13, doi:10.3390/w9110897, 2017.

Wani, J. M., Thayyen, R. J., Gruber, S., Ojha, C. S. P. and Stumm, D.: Single-year thermal regime and inferred permafrost occurrence in the upper Ganglass catchment of the cold-arid Himalaya, Ladakh, India, Sci. Total Environ., 703, doi:10.1016/j.scitotenv.2019.134631, 2020.

Westermann, S., Lüers, J., Langer, M., Piel, K. and Boike, J.: The annual surface energy budget of a high-arctic permafrost site on Svalbard, Norway, Cryosph., 3(2), 245–263, doi:10.5194/tc-3-245-2009, 2009.

Wickham, H.: ggplot2: Elegant Graphics for Data Analysis, [online] Available from: https://ggplot2.tidyverse.org, 2016.

Wickham, H.: tidyverse: Easily Install and Load the “Tidyverse”., [online] Available from: https://cran.r-project.org/package=tidyverse, 2017.

Wickham, H. and Francois, R.: dplyr: A Grammar of Data Manipulation, [online] Available from: https://cran.r-project.org/package=dplyr, 2016.

Wilke, C. O.: cowplot: Streamlined Plot Theme and Plot Annotations for “ggplot2,” [online] Available from: https://cran.r-project.org/package=cowplot, 2019.

Woo, M.-K., Kane, D. L., Carey, S. K. and Yang, D.: Progress in permafrost hydrology in the new millennium, Permafr. Periglac. Process., 19(2), 237–254, doi:10.1002/ppp.613, 2008.

Wünnemann, B., Reinhardt, C., Kotlia, B. S. and Riedel, F.: Observations on the relationship between lake formation, permafrost activity and lithalsa development during the last 20 000 years in the Tso Kar basin, Ladakh, India, Permafr. Periglac. Process., 19(4), 341–358, doi:10.1002/ppp.631, 2008.

Xia, Z.: Simulation of the Bare Soil Surface Energy Balance at the Tongyu Reference Site in Semiarid Area of North China, Atmos. Ocean. Sci. Lett., 3(6), 330–335, doi:10.1080/16742834.2010.11446892, 2010.

Yang, D., Goodison, B. E., Metcalfe, J. R., Louie, P., Leavesley, G., Emerson, D., Hanson, C. L., Golubev, V. S., Elomaa, E., Gunther, T., Pangburn, T., Kang, E. and Milkovic, J.: Quantification of precipitation measurement discontinuity induced by wind shields on national gauges, Water Resour. Res., 35(2), 491–508, doi:10.1029/1998WR900042, 1999.

Yao, J., Zhao, L., Ding, Y., Gu, L., Jiao, K., Qiao, Y. and Wang, Y.: The surface energy budget and evapotranspiration in the Tanggula region on the Tibetan Plateau, Cold Reg. Sci. Technol., 52(3), 326–340, doi:10.1016/j.coldregions.2007.04.001, 2008.

Yao, J., Zhao, L., Gu, L., Qiao, Y. and Jiao, K.: The surface energy budget in the permafrost region of the Tibetan Plateau, Atmos. Res., 102(4), 394–407, doi:10.1016/j.atmosres.2011.09.001, 2011.

Yao, J., Gu, L., Yang, C., Chen, H., Wang, J., Ding, Y., Li, R., Zhao, L., Xiao, Y., Qiao, Y., Shi, J. and Chen, C.: Estimation of surface energy fluxes in the permafrost region of the Tibetan Plateau based on situ measurements and the <scp>SEBS</scp> model, Int. J. Climatol., joc.6551, doi:10.1002/joc.6551, 2020.

Ye, Z. and Pielke, R. A.: Atmospheric Parameterization of Evaporation from Non-Plant-covered Surfaces, J. Appl. Meteorol., 32(7), 1248–1258, doi:10.1175/1520-0450(1993)032<1248:APOEFN>2.0.CO;2, 1993.

Zanotti, F., Endrizzi, S., Bertoldi, G. and Rigon, R.: The GEOTOP snow module, Hydrol. Process., 18(18), 3667–3679, doi:10.1002/hyp.5794, 2004.

Zhang, G., Kang, S., Fujita, K., Huintjes, E., Xu, J., Yamazaki, T., Haginoya, S., Wei, Y., Scherer, D., Schneider, C. and Yao, T.: Energy and mass balance of Zhadang glacier surface, central Tibetan Plateau, J. Glaciol., 59(213), 137–148, doi:10.3189/2013JoG12J152, 2013.

Zhao, L., Cheng, G., Li, S., Zhao, X. and Wang, S.: Thawing and freezing processes of active layer in Wudaoliang region of Tibetan Plateau, Chinese Sci. Bull., 45(23), 2181–2187, doi:10.1007/BF02886326, 2000.

Zhu, M., Yao, T., Yang, W., Maussion, F., Huintjes, E. and Li, S.: Energy- and mass-balance comparison between Zhadang and Parlung No. 4 glaciers on the Tibetan Plateau, J. Glaciol., 61(227), 595–607, doi:10.3189/2015JoG14J206, 2015.